CANCER

PARP2 deficiency impairs pancreatic cancer progression by promoting genomic instability and antitumor immunity

Neus Martínez-Bosch[1]†, Noemí Manero-Rupérez[2]†, Núria Vázquez-Bellón[3,4]†, Bennett Nickell-Hernández[2], Cristina Ventura-Blanch[3], Nura Lutfi[2], Carmen G. Lechuga[5,6], Carlos Martínez[7,8], Mireia Moreno[2], Coral Ampurdanés[2], Etna Abad[9], Mar Iglesias[2,6,10], María Muñoz-Escribano[1], Ana Janic[9], Meritxell Rovira[11,12], Carmen Guerra[5,6], Gabriel A. Rabinovich[13,14,15], José Yélamos[1,10]*, Pilar Navarro[1,3,16]*

Pancreatic cancer represents one of the most lethal tumors, characterized by an immunosuppressive microenvironment and a lack of cytotoxic immune cell infiltrates, which confer resistance to immunotherapy. Here, we demonstrate that deletion of poly(ADP-ribose) polymerase 2 (PARP2) in a *Myc*-driven mouse model of pancreatic cancer delays tumor progression and increases survival. Mechanistically, PARP2 loss induces enrichment of pathways associated with genomic instability and replicative stress, leading to increased γH2AX, chromosomal instability, and micronuclei accumulation. In addition to these tumor-intrinsic effects, PARP2 deletion reshapes the tumor microenvironment, promoting infiltration of cytotoxic T and natural killer cells while reducing immunosuppressive cell populations, enhancing antitumor cytotoxicity. These findings are recapitulated in a *Kras*^{G12D}-driven orthotopic pancreatic ductal adenocarcinoma model. Collectively, our data support selective PARP2 inhibition as a promising therapeutic strategy for pancreatic cancer by impairing genome integrity and boosting antitumor immune response, thereby opening potential avenues for combating this devastating disease.

INTRODUCTION

Pancreatic ductal adenocarcinoma (PDAC) stands out as one of the most aggressive tumors, ranking as the third leading cause of cancer-related deaths (*1*). This aggressiveness is tightly associated with several factors, including a dense fibrotic stroma, an intensely hypoxic environment, and an immunosuppressive microenvironment (*2*), which render PDAC highly resistant to therapy. The mutational landscape of PDAC includes activating mutations in the *KRAS* oncogene, alongside genetic alterations in pivotal tumor suppressor genes such as *TP53*, *CDKN2A*, and *SMAD4* (*2*). Furthermore, a growing body of evidence indicates that the dysregulation of the *MYC* oncogene plays a crucial role in the initiation, maintenance, and metastatic progression of PDAC (*3*–*5*). Notably, *KRAS* and *MYC* are major drivers of replicative stress (RS), which can fuel tumorigenesis by acting as a source of genomic instability and mutations (*6*). Accordingly, pancreatic cancer exhibits one of the highest levels of RS among tumors, which favors tumor progression and resistance to therapy, but can also represent an exploitable vulnerability in PDAC treatment. In this line, inhibitors targeting DNA damage responses, such as poly(ADP-ribose) polymerase 1/2 (PARP1/2) inhibitors (PARPi), offer promising avenues for exploiting this vulnerability (*7*).

PARP1 and PARP2 are the two enzymes of the PARP family of proteins that, in response to DNA damage, catalytically cleave β-NAD$^+$ [β-nicotinamide adenine dinucleotide (oxidized form)] to transfer adenosine 5′-diphosphate (ADP)–ribose moieties onto a variety of amino acid residues on acceptor proteins, creating long chains of poly(ADP-ribose) (PARylation) (*8*). Given their role in the DNA damage response, PARPi have become established cancer therapies for patients harboring homologous recombination-deficient tumors such as *BRCA1/2* mutants (*7*). In PDAC, PARPi are limited to a small subset of patients—less than 5%—with *BRCA1/2* mutations, and even among these, therapeutic efficacy remains notably limited (*9*).

Currently approved PARPi do not discriminate between PARP1 and PARP2, despite mounting evidence showing that these proteins fulfill distinct biological roles (*10*). Recent findings in a preclinical cancer model have demonstrated opposite roles for these enzymes: Loss of PARP2 prevents *Myc*-driven B cell lymphoma, whereas PARP1 deficiency promotes lymphomagenesis (*11*). In pancreatic cancer, previous data from our group demonstrated that PARP1 deletion does not affect tumor progression or animal survival, although modest effects on proliferation, apoptosis, angiogenesis, and acinar-to-ductal metaplasia (ADM) were observed (*12*). In contrast, the role of PARP2 in this tumor remains unknown.

[1]Cancer Research Program, Hospital del Mar Research Institute (HMRI), Unidad Asociada IIBB-CSIC, Barcelona, Spain. [2]Cancer Research Program, Hospital del Mar Research Institute (HMRI), Barcelona, Spain. [3]Institute of Biomedical Research of Barcelona (IIBB-CSIC), Barcelona, Spain. [4]PhD Program in Biomedicine, Facultat de Medicina (Campus Clínic), Universitat de Barcelona, Barcelona, Spain. [5]Experimental Oncology, Molecular Oncology Program, Centro Nacional de Investigaciones Oncológicas (CNIO), Madrid, Spain. [6]Centro de Investigación Biomédica en Red Cancer (CIBERONC), Madrid, Spain. [7]Experimental Pathology Unit, IMIB-LAIB-Arrixaca, Murcia, Spain. [8]Departamento de Anatomía y Anatomía Patológica Comparadas, Universidad de Murcia, Murcia, Spain. [9]Department of Medicine and Life Sciences, Universidad Pompeu Fabra, Barcelona, Spain. [10]Department of Pathology, Hospital del Mar, Barcelona, Spain. [11]Department of Physiological Science, School of Medicine, L'Hospitalet de Llobregat, University of Barcelona (UB), Barcelona, Spain. [12]Pancreas Regeneration: Pancreatic Progenitors and Their Niche Group, Institut d'Investigació Biomèdica de Bellvitge-IDIBELL, L'Hospitalet de Llobregat, Barcelona, Spain. [13]Laboratorio de Glicomedicina e Inmunopatología, Instituto de Biología y Medicina Experimental, Consejo Nacional de Investigaciones Científicas y Técnicas, Ciudad de Buenos Aires, Argentina. [14]Departamento de Química Biológica, Facultad de Ciencias Exactas y Naturales, Universidad de Buenos Aires, Ciudad de Buenos Aires, Argentina. [15]Laboratory of Glycoimmunology, CaixaResearch Institute, Barcelona, Spain. [16]Institut d'Investigacions Biomèdiques August Pi Sunyer (IDIBAPS), Barcelona, Spain.
*Corresponding author. Email: jyelamos@researchmar.net (J.Y.); pilar.navarro@iibb.csic.es, pnavarro@researchmar.net (P.N.)
†These authors contributed equally to this work.

Here, we aim to elucidate the role of PARP2 in pancreatic cancer using preclinical models of PDAC. We describe PARP2 overexpression in human PDAC and show that PARP2 deficiency notably affects tumor initiation and progression in a *Myc*-driven mouse model of pancreatic cancer, leading to a substantial reduction in tumor size and an increased survival rate. Transcriptomic and functional in vitro and in vivo analyses unveiled a key role of this protein in controlling genomic stability, RS, and immune evasion. These results were confirmed in a $Kras^{G12D}$-driven p53-deficient PDAC murine model, where depletion of PARP2 correlated with delayed tumor growth, enhanced genomic instability, and increased antitumor immune responses. Collectively, these findings underscore a crucial role of PARP2 in PDAC onset and progression, unveiling promising therapeutic avenues for leveraging selective PARP2 inhibitors to potentially reverse immunosuppression in pancreatic cancer and boost pancreatic antitumor immunity.

RESULTS

PARP2 is overexpressed in human pancreatic cancer

To explore the role of PARP2 in pancreatic cancer, we first assessed PARP2 protein expression by immunohistochemistry in a panel of human PDAC samples and healthy tissue (table S1). Ductal tumor cells showed higher PARP2 staining, localizing preferentially in the nucleus, compared with normal tissue, which exhibited a faint cytosolic signal in acinar cells (Fig. 1A). This distribution contrasts with that of PARP1, which localizes to the nucleus of normal acinar cells and shows negative or faint expression in PDAC (fig. S1A) (*12*). In addition to tumor cells, infiltrating immune cells within the tumor microenvironment also expressed PARP2 (Fig. 1A). Quantitative assessment using the H-score method confirmed a significant increase in PARP2 expression in tumor samples relative to normal pancreatic tissue, supporting its overexpression in the malignant context (Fig. 1A).

To gain further insight into PARP2 expression in normal and tumor pancreatic tissues, we conducted an analysis of mRNA expression levels in healthy human pancreatic tissue and tumor samples sourced from the Genotype-Tissue Expression (GTEx) and The Cancer Genome Atlas (TCGA) datasets. This analysis showed that PARP2 mRNA expression was significantly increased in pancreatic tumors compared with normal tissue (Fig. 1B). Moreover, stratification of TCGA pancreatic tumors according to their molecular signatures revealed higher PARP2 expression levels in the squamous tumor subtype (Fig. 1C), which is associated with very poor prognosis (*13*). To further understand the role of PARP2 in PDAC biology, we categorized human TCGA tumors based on their PARP2 mRNA expression levels into low (quartile 1) or high (quartile 4) PARP2 expression groups and assessed their survival outcomes. The 1-year survival rate was 81.6% (31 of 38) for patients with low PARP2 expression, while it decreased to 55.3% (21 of 38) for those with high levels ($P < 0.05$, Fisher's exact test). Gene Set Enrichment Analysis (GSEA) revealed significant differences for important biological processes related to tumorigenesis when comparing patients with high or low PARP2 expression, including cell chemotaxis and extravasation, immune responses, DNA replication, mitotic nuclear division, and chromosome segregation (Fig. 1D and data S1). Together, these results indicate that PARP2 is overexpressed in human PDAC—more prominently in the squamous tumor subtype—and is associated with aggressiveness and poor prognosis.

PARP2 deletion delays tumor onset and progression in a *Myc*-driven pancreatic cancer mouse model

Given the association of PARP2 overexpression with PDAC and poor patient survival, we hypothesized that PARP2 may exert an oncogenic role in this cancer. To investigate this hypothesis, we used a preclinical approach by crossing the pancreatic cancer mouse model Ela-Myc with a PARP2 knockout mouse ($PARP2^{-/-}$) and monitored tumor development. Myc deregulation is frequent in human PDAC, and multiple in vivo mouse studies have demonstrated its crucial role in tumor initiation and maintenance (*3*–*5*). The pancreatic cancer mouse model Ela-Myc overexpresses c-Myc under the acinar-specific elastase promoter and develops PDAC after undergoing ADM, a key process in human PDAC initiation (*14*). Immunohistochemical characterization of Ela-Myc–derived tumors revealed high levels of PARP2 expression in the nucleus, mirroring the expression pattern of human PDAC (Fig. 2A). Moreover, PARP2 and c-Myc exhibited overlapping spatial distribution patterns in adjacent serial sections, both in Ela-Myc–derived pancreatic tumors and in human PDAC, highlighting that this model recapitulates human disease (Fig. 2A).

Mice were euthanized when tumor reached predefined ethical endpoints (Fig. 2B). Kaplan-Meier survival curves showed that loss of both alleles of PARP2 in Ela-Myc mice (EMyc:$PARP2^{-/-}$) resulted in a significant 43% increase in animal life span, compared with control Ela-Myc (EMyc:$PARP2^{+/+}$) mice (Fig. 2C). The median survival increased from 137 days in EMyc:$PARP2^{+/+}$ mice to 196 days in EMyc:$PARP2^{-/-}$ mice ($P < 0.001$, log-rank test). Notably, 75% of EMyc:$PARP2^{-/-}$ mice belonged to the long-term survivor group (mice surviving longer than 6 months), compared with only 14% of EMyc:$PARP2^{+/+}$ mice (Fig. 2D). Histological characterization of endpoint pancreatic tumors from EMyc:$PARP2^{+/+}$ and EMyc:$PARP2^{-/-}$ mice showed increased levels of DNA damage (γH2AX staining) and apoptosis (cleaved caspase-3) in tumors lacking PARP2, with no discernible differences noted in terms of proliferation [using the mitotic marker phospho-histone H3 (Ser^{10})] or necrosis (fig. S1B). Additional characterization of these endpoint tumors showed a highly significant reduction in the percentage of ductal tumor lesions in EMyc:$PARP2^{-/-}$ compared with EMyc:$PARP2^{+/+}$ mice (8.7 versus 38.7%) (Fig. 2E). These data indicate that PARP2 participates in pancreatic ADM and its loss impairs acinar reprogramming toward a ductal phenotype. End-stage tumors of EMyc:$PARP2^{-/-}$ and EMyc:$PARP2^{+/+}$ mice exhibited a similar metastatic burden (fig. S1C).

To assess whether the increased survival observed in EMyc:$PARP2^{-/-}$ mice was related to delayed tumor onset, we performed time-course analysis of young (3- and 4-month-old) animals (Fig. 2F). Three-month-old mice of both genotypes were euthanized and analyzed for the presence of preneoplastic lesions and/or tumors (Fig. 2G). While 90% of EMyc:$PARP2^{+/+}$ showed macroscopic tumors, only 10% of EMyc:$PARP2^{-/-}$ did (Fig. 2G). Microscopic examination indicated that 100% of EMyc:$PARP2^{+/+}$ mice developed pancreatic tumors, versus only 50% of EMyc:$PARP2^{-/-}$ mice, whereas the remaining 50% had acinar atrophy (20%) or no microscopic pancreatic lesions (30%) (fig. S1D). Similarly, tumors from 4-month-old EMyc:$PARP2^{-/-}$ mice were significantly smaller compared with EMyc:$PARP2^{+/+}$ mice (Fig. 2H). At the 4-month time point, PARP2 deficiency led to a significant reduction of metastases in EMyc:$PARP2^{-/-}$ compared with EMyc:$PARP2^{+/+}$ control mice (Fig. 2I).

Together, these results indicate that PARP2 plays a protumorigenic role in *Myc*-driven pancreatic cancer. Its genetic deletion not only increases survival, but also modulates acinar cell plasticity and hampers tumor onset and progression.

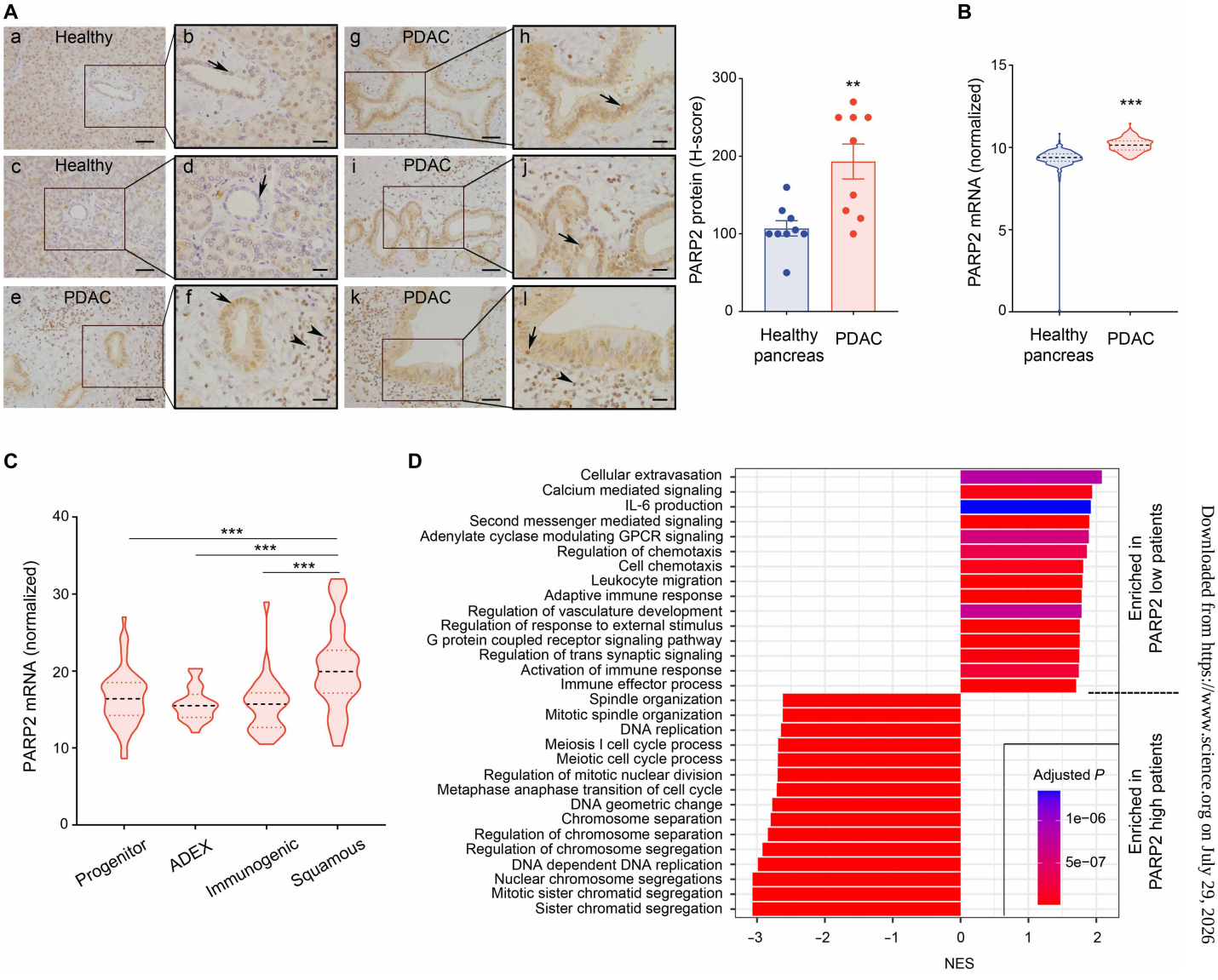

Fig. 1. PARP2 expression in human pancreatic cancer. (**A**) Left: Representative images of PARP2 protein expression detected by immunohistochemistry in healthy pancreatic tissue [(a) to (d)] and in human PDAC lesions [(e) to (l)]. Arrows indicate ductal cells and arrowheads mark immune infiltrates. Scale bars, 50 μm [(a), (c), (e), (g), (i), and (k)] and 20 μm [(b), (d), (f), (h), (j), and (l)]. Right: H-score quantification of PARP2 expression ($N = 9$ healthy pancreas; $N = 9$ PDAC). (**B**) PARP2 mRNA levels in pancreatic tissue samples from the GTEx and TCGA datasets, including 171 normal pancreas (167 samples from GTEx and 4 samples from TCGA) and 150 tumors (from the TCGA database). Raw count data were normalized using DESeq2. (**C**) PARP2 mRNA expression in different human PDAC molecular subtypes: pancreatic progenitor ($N = 51$), aberrantly differentiated endocrine exocrine (ADEX; $N = 37$), immunogenic ($N = 27$), and squamous ($N = 31$). Raw mRNA count data were retrieved from TCGA database and normalized using the trimmed mean of M values (TMM) method. (**D**) Most significant gene ontology (GO) biological processes enriched in TCGA PDAC tumors with low PARP2 expression ($N = 38$; quartile 1) versus high PARP2 expression ($N = 38$; quartile 4). Pathways are ordered by normalized enrichment score (NES) and adjusted *P* values indicated by color scale. $^{**}P < 0.01$; $^{***}P < 0.001$, Mann-Whitney *U* test.

Last, we examined whether PARP1 levels were altered following PARP2 loss. We assessed PARP1 expression in EMyc:PARP2$^{+/+}$ and EMyc:PARP2$^{-/-}$ mice by immunohistochemistry (fig. S1E) and Western blot (fig. S1F), revealing no compensatory up-regulation in the absence of PARP2. Moreover, given that current therapeutic strategies often target both PARP1 and PARP2, we investigated whether treatment with the PARP1/2 inhibitor olaparib could mimic or enhance the tumor-suppressive effects observed in PARP2-deficient mice. Olaparib treatment of EMyc:PARP2$^{+/+}$ and EMyc:PARP2$^{-/-}$ mice did not lead to significant differences in tumor incidence (fig. S1G) or tumor burden (fig. S1H) compared with vehicle-treated controls, indicating that dual PARP1/2 inhibition does not recapitulate or enhance the effects of PARP2 deficiency in this model.

Overall, our results highlight a tumor-promoting role that is specific to PARP2 and underscore the relevance of selectively targeting PARP2 in pancreatic cancer, at least within the context of the *Myc*-driven model.

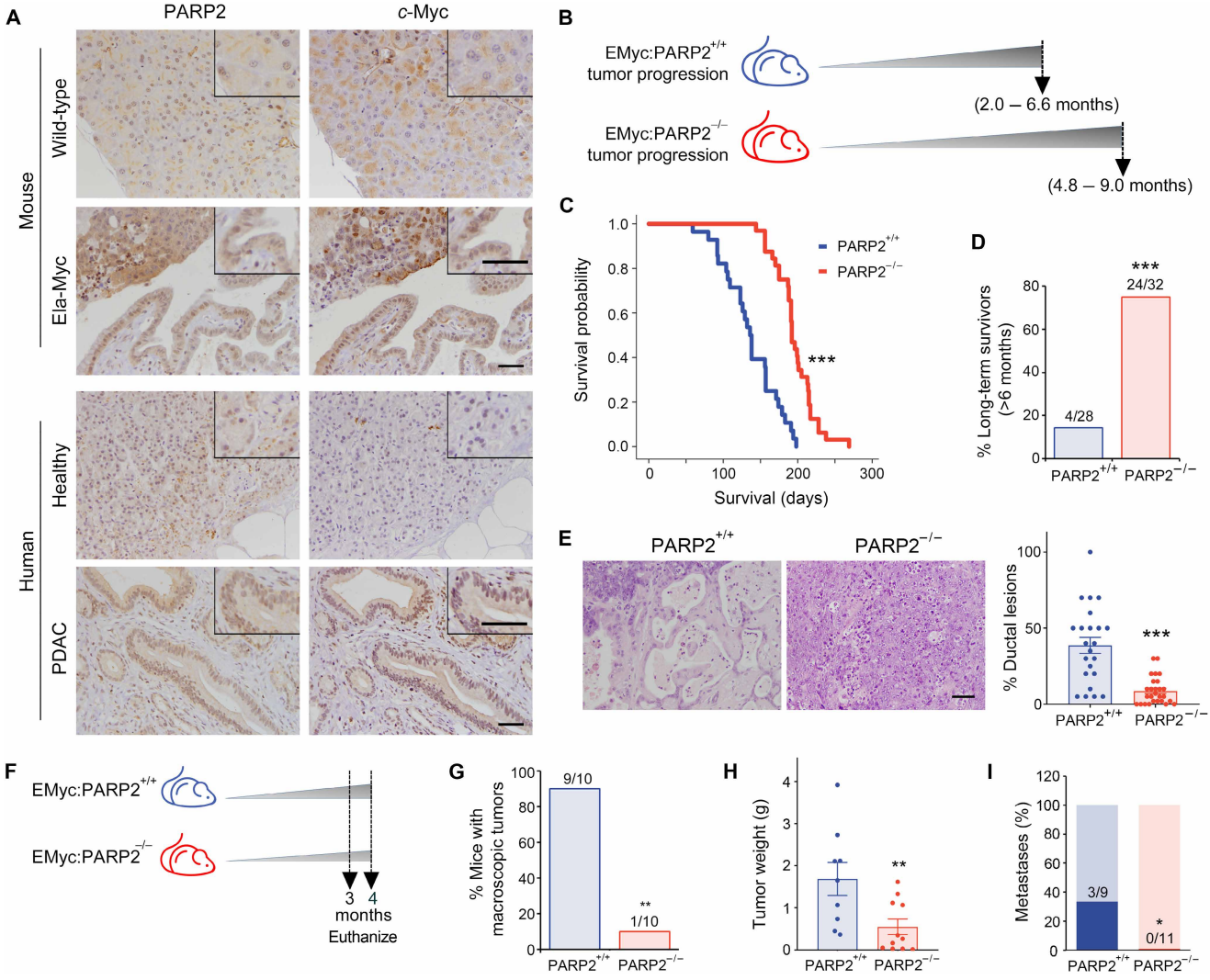

Fig. 2. PARP2 deficiency delays *Myc*-driven pancreatic cancer progression in mice. (**A**) Representative images showing PARP2 and c-Myc protein detection in mouse and human pancreatic samples, evaluated by immunohistochemistry in serial tissue sections. Healthy mouse tissue is from C57BL/6 (wild-type) mice, and tumor tissue is from Ela-Myc mice; human samples include healthy and tumor pancreatic tissues. Scale bars, 50 μm. (**B**) Schematic representation of tumor progression in EMyc:PARP2$^{+/+}$ and EMyc:PARP2$^{-/-}$ mice, indicating the endpoint referenced in (C) to (E). (**C**) Kaplan-Meier survival curves for EMyc:PARP2$^{+/+}$ ($N = 28$) and EMyc:PARP2$^{-/-}$ ($N = 32$) mice. ***$P < 0.001$, log-rank test. (**D**) Percentage of EMyc:PARP2$^{+/+}$ ($N = 28$) and EMyc:PARP2$^{-/-}$ ($N = 32$) mice that survived longer than 6 months. ***$P < 0.001$, Fisher's exact test. (**E**) Left: Representative hematoxylin and eosin (H&E) staining of EMyc:PARP2$^{+/+}$ and EMyc:PARP2$^{-/-}$ pancreatic tumors. Right: Percentage of ductal component calculated for each tumor, presented as mean values for each group; EMyc:PARP2$^{+/+}$ ($N = 23$) and EMyc:PARP2$^{-/-}$ ($N = 27$) mice. ***$P < 0.001$, Mann-Whitney *U* test. (**F**) Schematic representation of the early-stage analysis (3 or 4 months) in EMyc:PARP2$^{+/+}$ and EMyc:PARP2$^{-/-}$, referenced in (G) to (I). (**G**) Percentage of 3-month-old tissue from EMyc:PARP2$^{+/+}$ ($N = 10$) and EMyc:PARP2$^{-/-}$ ($N = 10$) mice that presented macroscopic tumors at necropsy. **$P < 0.01$, Fisher's exact test. (**H**) Tumor weight of 4-month-old EMyc:PARP2$^{+/+}$ ($N = 9$) and EMyc:PARP2$^{-/-}$ ($N = 11$) mice. **$P < 0.01$, Mann-Whitney *U* test. (**I**) Analysis of metastasis in 4-month-old EMyc:PARP2$^{+/+}$ ($N = 9$) and EMyc:PARP2$^{-/-}$ ($N = 11$) mice. Data are presented as the percentage of animals per experimental group exhibiting metastases (scored as positive if at least one histologically confirmed metastatic lesion was detected). *$P < 0.05$, chi-square test.

PARP2 deficiency induces genomic instability in a *Myc*-driven pancreatic cancer mouse model

To investigate the molecular mechanisms of PARP2 functions in pancreatic cancer, we performed transcriptomic analysis by RNA sequencing (RNA-seq) of pancreatic samples from young age-matched (3-month-old) EMyc:PARP2$^{+/+}$ and EMyc:PARP2$^{-/-}$ mice. Bioinformatics analyses showed, with a false discovery rate (FDR) cutoff of 1%, 1580 up-regulated genes and 964 down-regulated genes in EMyc:PARP2$^{-/-}$ compared with EMyc:PARP2$^{+/+}$ (data S2 and fig. S2, A and B). GSEA of these data revealed multiple up-regulated and down-regulated pathways associated with key tumor-related biological processes (Fig. 3A and data S3). Notably, many of these pathways were also identified in the GSEA data from human samples in the TCGA analysis (Fig. 1D), highlighting a shared molecular signature between the mouse model and human cancer data (Fig. 3B and data S4).

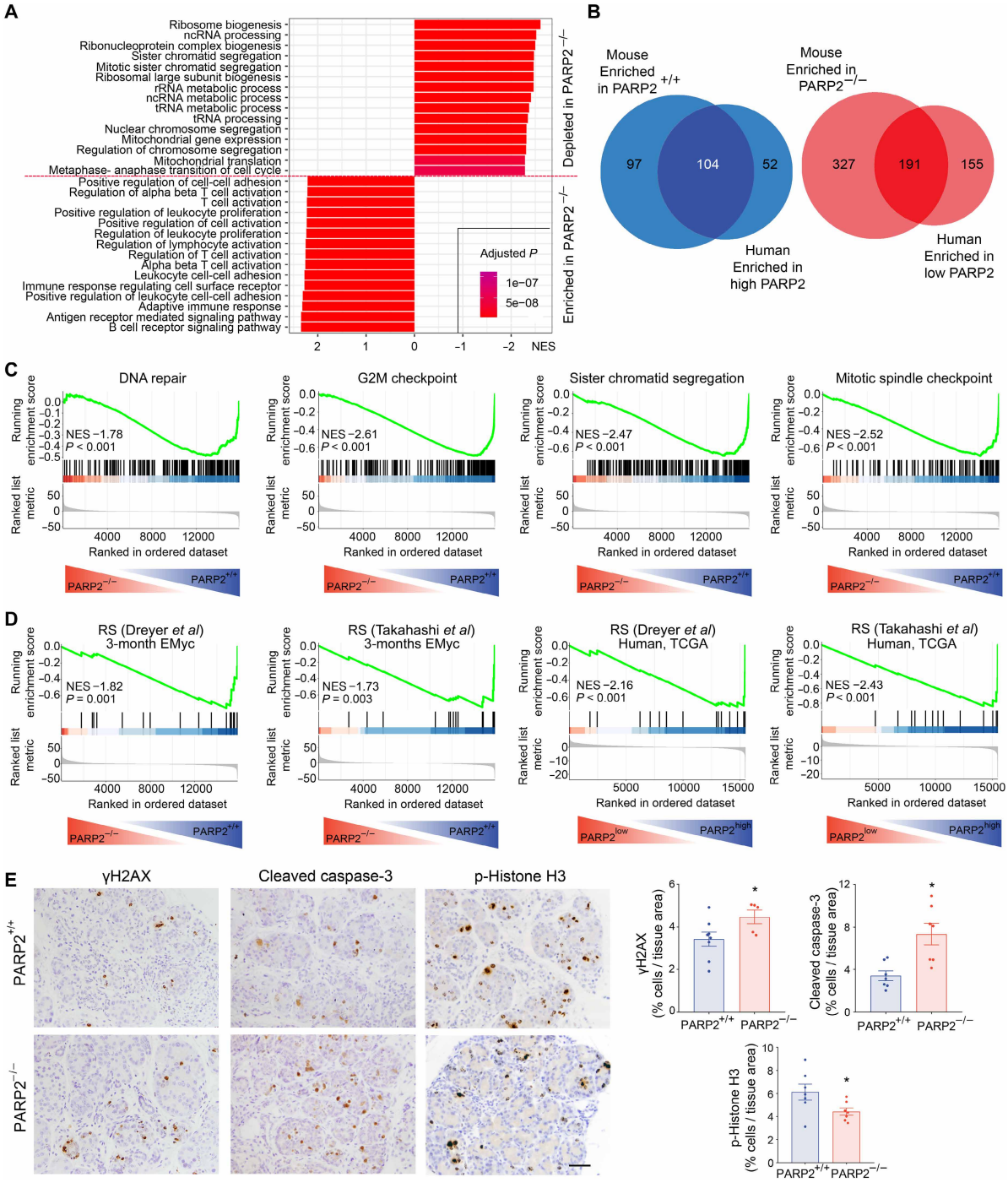

Fig. 3. Molecular characterization of PARP2 depletion in Ela-Myc 3-month-old pancreatic tissue. (**A**) GSEA of RNA-seq data showing pathways significantly depleted or enriched in 3-month-old pancreatic samples from EMyc:PARP2$^{-/-}$ ($N = 3$) compared with EMyc:PARP2$^{+/+}$ ($N = 3$) mice. Pathways are ranked by NES, and adjusted P values are indicated by color scale. (**B**) Venn diagrams showing overlap of GO biological process terms in human samples with low PARP2 expression ($N = 38$ patients; quartile 1) versus murine EMyc:PARP2$^{-/-}$ samples ($N = 3$ mice) and in human samples with high PARP2 expression ($N = 38$ patients; quartile 4) versus murine EMyc:PARP2$^{+/+}$ samples ($N = 3$ mice). (**C**) GSEA plots for DNA repair, G2M checkpoint, sister chromatid segregation, and mitotic spindle checkpoint, comparing 3-month-old EMyc:PARP2$^{-/-}$ ($N = 3$ mice) to EMyc:PARP2$^{+/+}$ pancreatic samples ($N = 3$ mice). NES and adjusted P values are shown on the plots. (**D**) RS enrichment plots using the signature described in Dreyer *et al.* (*16*) or Takahashi *et al.* (*17*) in murine 3-month-old EMyc:PARP2$^{+/+}$ ($N = 3$ mice) and EMyc:PARP2$^{-/-}$ ($N = 3$ mice) pancreatic tissue, and in human TCGA samples ($N = 38$ patients in quartile 1 versus $N = 38$ patients in quartile 4). NES and adjusted P values are shown. (**E**) Representative immunohistochemistry images (left) and quantification (right) showing the percentage of cells positive for markers of DNA damage (γH2AX), apoptosis (cleaved caspase-3), and proliferation [phospho-histone H3 (Ser^{10})] in 3-month-old EMyc:PARP2$^{+/+}$ pancreatic tissue ($N = 8$, 7, and 7 mice, respectively) and EMyc:PARP2$^{-/-}$ tissue ($N = 5$, 7, and 7 mice, respectively). Scale bar, 50 μm. $^{*}P < 0.05$; $^{**}P < 0.01$, Mann-Whitney U test.

Transcriptomic profiling of PARP2-deficient tumors revealed significant down-regulation of pathways involved in DNA repair, mitosis, and chromosome segregation (Fig. 3C). Considering the crucial role of PARP2 in the cellular response to RS (*15*), we analyzed RNA-seq data using independent RS signatures previously identified in PDAC (*16*, *17*). Consistently, EMyc:PARP2$^{-/-}$ samples exhibited down-regulation of RS response pathways (Fig. 3D), suggesting an impaired ability to cope with oncogene-induced RS. This effect was further corroborated using RNA-seq data from human PDAC samples in the TCGA dataset (Fig. 3D). Altered expression of RS signature genes (*Aurka*, *Cdca5*, *E2f1*, and *Mybl2*) was also confirmed by reverse transcription quantitative polymerase chain reaction (RT-qPCR) (fig. S2C). Moreover, immunohistochemical analysis of preneoplastic pancreas from 3-month-old mice showed increased γH2AX staining in PARP2-deficient cells compared with EMyc:PARP2$^{+/+}$ samples (Fig. 3E), in agreement with the role of PARP2 in the DNA damage response. We also found decreased proliferation, as assessed by phospho-histone H3 (Ser^{10}) positive nuclei, and increased apoptosis, reflected by increased cleaved caspase-3 staining in pancreas tissue sections from EMyc:PARP2$^{-/-}$ versus EMyc:PARP2$^{+/+}$ mice (Fig. 3E). To further investigate the involvement of PARP2 in genomic instability, we performed metaphase chromosome spread analysis of cells derived from EMyc:PARP2$^{+/+}$ and EMyc:PARP2$^{-/-}$ end-stage tumors. Notably, EMyc:PARP2$^{-/-}$ cells exhibited a significant increase in chromosome number compared with EMyc:PARP2$^{+/+}$ cells (Fig. 4A), indicating that PARP2 plays a critical role in maintaining chromosomal integrity under oncogenic stress. In addition, immunofluorescence analysis in these cell lines also revealed a significant increase in micronuclei formation detected by cytosolic double-stranded DNA (dsDNA) signal in PARP2-deficient tumor cells, accompanied by enhanced colocalization of cyclic guanosine 5′-monophosphate–adenosine 5′-monophosphate synthase (cGAS) (Fig. 4B and fig. S2D).

Despite the accumulation of RS and genomic instability, PARP2-deficient tumors in the Ela-Myc transgenic model do progress. Considering the pivotal role of p53 as a guardian of genome integrity and that *Trp53* haploinsufficiency was shown to overcome the lymphoma delay caused by loss of PARP2 in a *Myc*-driven lymphoma model (*11*), we next investigated the role of the p53 pathway in our Ela-Myc pancreatic cancer model. To this aim, we analyzed the p53 status in pancreatic samples from 3-month-old EMyc:PARP2$^{+/+}$ and EMyc:PARP2$^{-/-}$ mice by performing a transcriptomic assessment of p53 pathway activity using the Pathway RespOnsive GENes for activity inference (PROGENy)

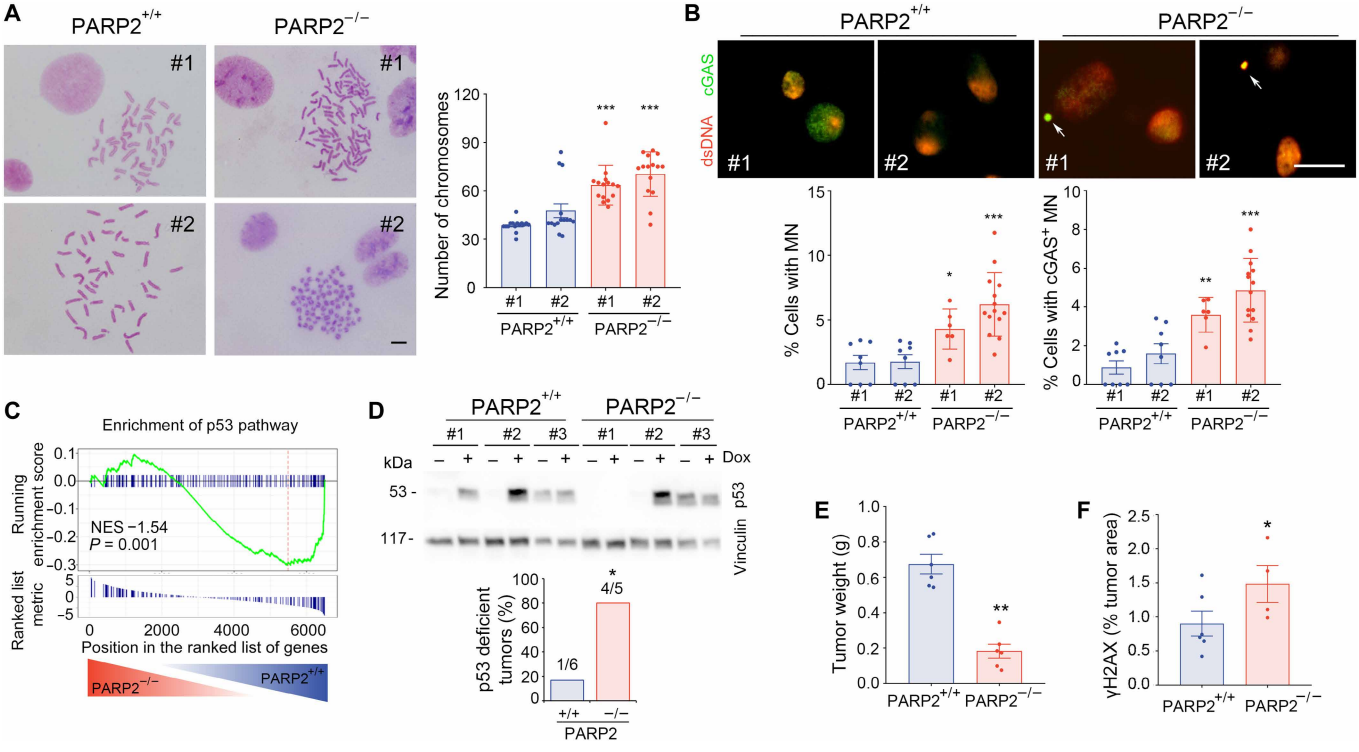

Fig. 4. PARP2 deficiency in Ela-Myc mice induces genomic instability, altered p53 pathway activity, and increased DNA damage. (**A**) Left: Representative metaphase spreads from primary tumor cell lines of EMyc:PARP2$^{+/+}$ (#1 and #2) and EMyc:PARP2$^{-/-}$ (#1 and #2) mice. Scale bar, 10 μm. Right: Quantification of chromosome number per cell ($N = 15$ metaphase spreads analyzed per cell line). ***$P < 0.001$, Mann-Whitney *U* test. (**B**) Top: Representative immunocytofluorescence images of micronuclei (MN), detected by dsDNA (red), and cGAS (green) in two primary cell lines derived from EMyc:PARP2$^{+/+}$ and from EMyc:PARP2$^{-/-}$ tumors. Scale bar, 20 μm. Bottom: Percentage of cells with micronuclei, defined by cytosolic dsDNA staining (left) or positive for dsDNA and cGAS (right). Data represent percentage of cells from a minimum of 400 cells analyzed per group. **$P < 0.01$; ***$P < 0.001$, unpaired Student's *t* test. (**C**) Enrichment plot of the p53 pathway using PROGENy. NES and adjusted *P* values are shown. (**D**) Top: Representative Western blot of p53 protein levels following DNA damage induction with doxorubicin, in primary pancreatic tumor cells derived from EMyc:PARP2$^{+/+}$ ($N = 3$) and EMyc:PARP2$^{-/-}$ ($N = 3$) endpoint tumors. Vinculin is shown as a loading control. Bottom: Percentage of cell lines from EMyc:PARP2$^{+/+}$ ($N = 6$) and EMyc:PARP2$^{-/-}$ ($N = 5$) tumors exhibiting p53 deficiency. *$P < 0.05$, chi-square test. (**E**) Pancreatic tumor weight measured 5 weeks after orthotopic implantation of EMyc control or PARP2-knockout cells in immunodeficient NSG mice ($N = 6$ mice per group). **$P < 0.01$, Mann-Whitney *U* test. (**F**) Quantification of γH2AX immunohistochemistry to evaluate DNA damage in tumors derived from control ($N = 6$ tumors) or PARP2-knockout EMyc ($N = 4$ tumors) cells. *$P < 0.05$, unpaired Student's *t* test.

algorithm (*18*). This analysis revealed higher levels of p53 pathway activation in PARP2-deficient samples compared with controls (Fig. 4C; fig. S2, E and F; and data S5). Since PARP2 loss increases DNA damage and RS, this early up-regulation of the p53 pathway likely reflects a protective response aimed at eliminating damaged cells through apoptosis. These observations in early PARP2-deficient lesions raised the possibility that strong selective pressure exists to disable p53 as tumors progress in the absence of PARP2. To explore this hypothesis, we examined primary tumor cells derived from end-stage tumors by assessing their capacity to activate p53 in response to treatment with the DNA-damaging agent doxorubicin, a well-established inducer of p53 protein stabilization and activation. Eighty percent of EMyc:PARP2$^{-/-}$ tumors (4 of 5) failed to up-regulate p53 in response to treatment, consistent with loss of p53 function, whereas only 16.6% (1 of 6) EMyc:PARP2$^{+/+}$ tumors showed this deficiency ($P < 0.05$; Fig. 4D). These results suggest that inactivation of *Trp53*, either through loss of heterozygosity or truncating mutations leading to unstable protein or a missense/stabilizing mutation that leads to high steady-state levels of mutant p53 (Fig. 4D), is a common event in tumors arising in the absence of PARP2, suggesting that PARP2 loss imposes a selective pressure to inactivate p53 during tumor progression. This likely represents a compensatory mechanism that allows tumor cells to tolerate the increased RS associated with PARP2 loss and to sustain *Myc*-driven cancer progression.

Last, to directly assess the tumor-intrinsic contribution of PARP2 loss to RS and tumor growth in vivo, we used CRISPR-Cas9 to genetically deplete PARP2 from EMyc:PARP2$^{+/+}$ cells and orthotopically implanted PARP2$^{+/+}$ and PARP2$^{-/-}$ Ela-Myc CRISPR cell lines into immunodeficient NOD.Cg-Prkdc^{scid} Il2rg^{tm1Wjl}/SzJ (NSG) mice. Notably, tumors derived from PARP2-deficient cells exhibited significantly reduced growth compared with controls (Fig. 4E), confirming a strong cell-autonomous effect. Immunohistochemical analysis of tumor sections revealed increased γH2AX staining in PARP2$^{-/-}$ tumors (Fig. 4F), consistent with elevated DNA damage and RS, while levels of cleaved caspase-3 and phospho-histone H3 (Ser^{10}) were not significantly altered (fig. S2G).

Together, these results demonstrate that PARP2 genetic deletion leads to overall genomic instability, characterized by increased DNA damage, aberrant chromosomal organization, and accumulation of cytosolic DNA. These alterations likely impose a selective pressure for p53 inactivation as a compensatory mechanism during the progression of EMyc:PARP2$^{-/-}$ tumors. Moreover, loss of PARP2 in tumor cells is sufficient to impair tumor growth in vivo in an immunodeficient model, confirming a tumor-intrinsic role.

PARP2 deficiency triggers an antitumor immune response in a *Myc*-driven pancreatic cancer mouse model

In addition to the down-regulation of DNA repair and genomic stability–related pathways in pancreatic samples from EMyc:PARP2$^{-/-}$ mice, GSEA revealed that several of the most up-regulated biological processes were related to immune regulation. These included B cell receptor signaling, antigen receptor–mediated signaling, adaptive immune response, and positive regulation of leukocyte cell-cell adhesion, among others (Fig. 3A and data S3). Hallmark gene set analysis further found a significant enrichment in interferon-α, interferon-γ, inflammatory responses, and interleukin-6 (IL-6), Janus kinase (JAK), and signal transducer and activator of transcription (STAT) signaling (Fig. 5A). We validated by RT-qPCR several interferon-γ–related genes including *Irf1*, *Irf4*, *Irf8*, and *Il7*, which were significantly up-regulated after PARP2 depletion (fig. S3A). In addition, PARP2 deficiency also induced up-regulation of genes related to stimulator of interferon genes (STING) pathway including *Ifnb1*, *Ccl5*, and *Cxcl10* (fig. S3B). GSEA revealed an important overlap between the immune-related processes enriched in EMyc:PARP2$^{-/-}$ pancreatic samples and those found in PDAC samples with low PARP2 expression (Figs. 1D and 3, A and B; and data S4), suggesting a conserved immunomodulatory role for PARP2 across species.

Prompted by these transcriptomic signatures and the well-established role of immune surveillance in PDAC, we sought to gain further insight into PARP2-mediated modulation of the immune microenvironment in the Ela-Myc model. To this aim, we performed a cell deconvolution analysis with Immune Cell Abundance Identifier for mouse (ImmuCellAI-mouse) (*19*). We found an increase of CD4 T cells, CD8 T cells, B cells and natural killer (NK) cells, while regulatory T cells (T_{reg} cells) and protumor M2 macrophages were decreased in EMyc:PARP2$^{-/-}$ pancreatic samples compared with EMyc:PARP2$^{+/+}$ (Fig. 5B and fig. S3C). These results were validated by immunostaining of pancreatic tissue sections from 3-month-old mice of both genotypes using immune cell–specific markers. Increased number of CD4, CD8 T cells, and CD20 B cells and decreased number of protumor Foxp3^{+} cells and Arg1^{+} macrophages were found in EMyc:PARP2$^{-/-}$ preneoplastic samples compared with EMyc:PARP2$^{+/+}$ (Fig. 5C and fig. S3D). Tumor histology from 4-month-old mice confirmed decreased protumor Foxp3^{+} cells and Arg1^{+} macrophage populations in samples from EMyc:PARP2$^{-/-}$ mice in comparison to EMyc:PARP2$^{+/+}$ genotype (Fig. 5C).

To functionally determine the cytotoxic potential of PARP2$^{+/+}$ or PARP2$^{-/-}$ immune cells, we performed coculture assays using total splenocytes isolated from PARP2$^{+/+}$ or PARP2$^{-/-}$ mice and cocultured with corresponding EMyc:PARP2$^{+/+}$ or EMyc:PARP2$^{-/-}$ tumor cells for 4 hours (Fig. 5D). Splenocytes from PARP2$^{-/-}$ hosts exhibited heightened cytotoxic activity against both tumor genotypes (Fig. 5E and fig. S4), suggesting that PARP2 deficiency in immune cells boosts an antitumor effector function. Given the short duration of the assay, and the increased representation of NK cells observed in our prior immune cell deconvolution analysis (Fig. 5B), we next focused on NK cells as likely mediators of this effect. Purified NK cells from PARP2$^{-/-}$ hosts also demonstrated significantly increased cytotoxicity toward both tumor genotypes (Fig. 5F), confirming enhanced immune response upon PARP2 loss in this compartment.

Together, these results indicate that selective PARP2 deficiency reshapes the tumor immune microenvironment in pancreatic cancer, reducing immunosuppressive populations and enhancing cytotoxic responses.

PARP2 deletion impairs tumor progression in a *Kras^{G12D}*-driven pancreatic cancer mouse model

To broaden our investigation of PARP2 function in PDAC, we turned to a *Kras^{G12D}*-driven and p53-deficient tumor model (KPC), as oncogenic *KRAS* is the most prevalent genetic alteration in human PDAC (*2*). We first analyzed by immunohistochemistry the expression patterns of c-Myc, PARP1, and PARP2 in pancreatic tumors from *Kras^{G12D}*-driven mice, confirming that they resembled those observed in the Ela-Myc model, with robust PARP2 expression coexisting with high c-Myc levels and undetectable staining for PARP1 (Fig. 6A). Next, to examine the role of PARP2 in the *Kras^{G12D}*-driven PDAC model, we depleted PARP2 in KPC cells using CRISPR-Cas9 gene editing (fig. S5A) and investigated the effects of PARP2 loss in genomic instability. KPC:PARP2$^{-/-}$ cells showed increased total γH2AX and pan-nuclear

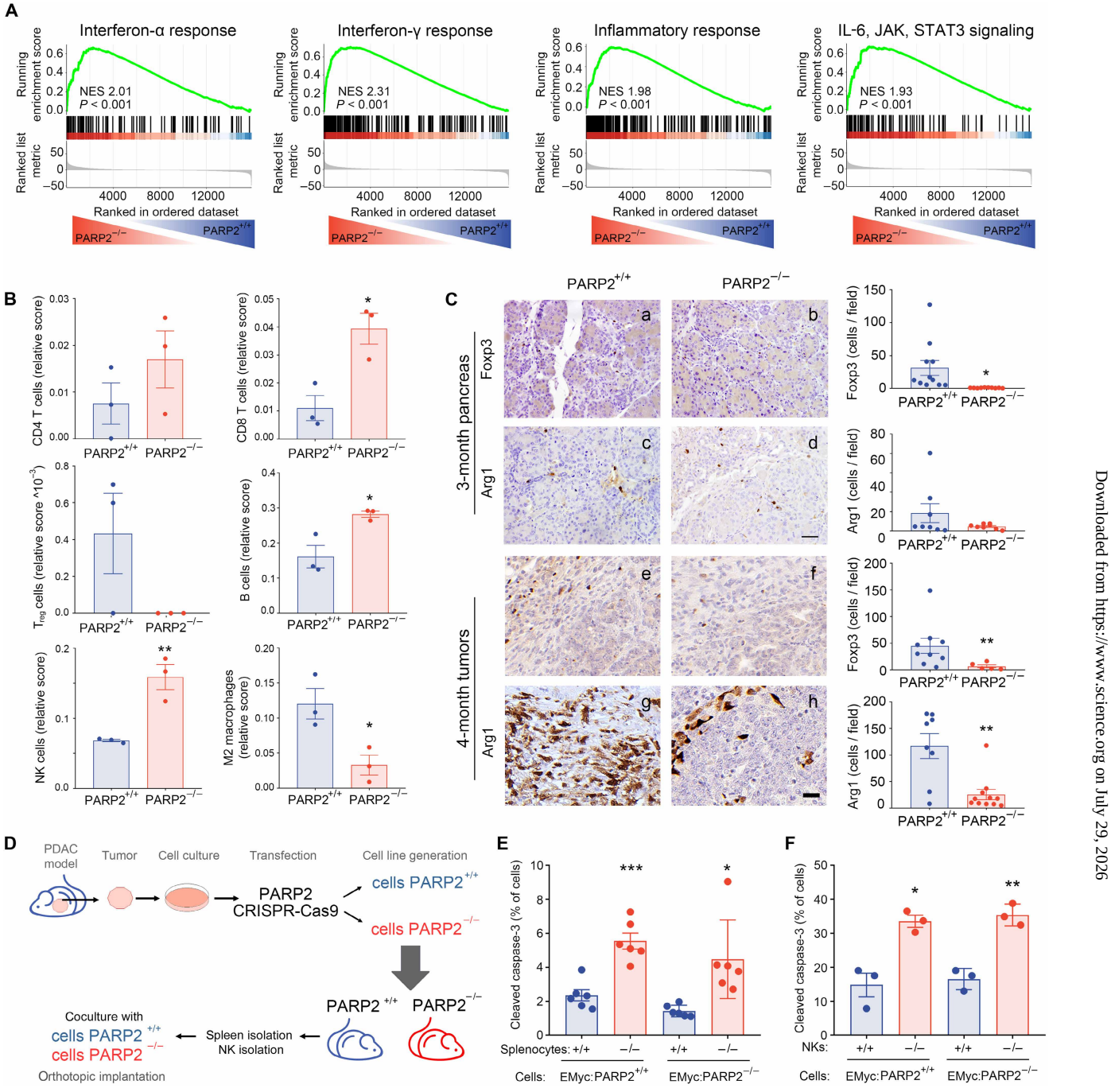

Fig. 5. PARP2 depletion induces an antitumor immune response in pancreatic tissue. (**A**) GSEA plots for interferon-α, interferon-γ, inflammatory response, and IL-6–JAK–STAT pathways in pancreatic samples from 3-month-old EMyc:PARP2$^{-/-}$ and EMyc:PARP2$^{+/+}$ mice ($N = 3$ per group). NES and adjusted P values are shown. (**B**) Relative abundance of CD4$^+$ and CD8$^+$ T cells, B cells, T_{reg} cells, NK cells, and M2 macrophages in EMyc:PARP2$^{+/+}$ and EMyc:PARP2$^{-/-}$ pancreatic tissue ($N = 3$ mice per group), determined by RNA-seq deconvolution. *$P < 0.05$; **$P < 0.01$, Student's t test. Comparisons without asterisks are not significant. (**C**) Representative images (left) and quantification (right) of immunohistochemical staining for Foxp3$^+$ cells in 3-month-old pancreatic tissue ($N = 11$ PARP2$^{+/+}$, $N = 10$ PARP2$^{-/-}$ mice) and 4-month-old tumors ($N = 9$ PARP2$^{+/+}$, $N = 5$ PARP2$^{-/-}$ mice), and for Arg1$^+$ cells in 3-month-old tissue ($N = 8$ PARP2$^{+/+}$, $N = 8$ PARP2$^{-/-}$ mice) and 4-month-old tumors ($N = 8$ PARP2$^{+/+}$, $N = 11$ PARP2$^{-/-}$ mice). Scale bars, 50 μm [(a) to (d)] and 25 μm [(e) to (h)]. *$P < 0.05$; **$P < 0.01$, Mann-Whitney U test. Comparisons without asterisks are not significant. (**D**) Schematic representation of the cytotoxicity assay using primary cell lines derived from PDAC mouse models. Splenocytes or NKs isolated from PARP2$^{+/+}$ or PARP2$^{-/-}$ mice were cocultured with PARP2$^{+/+}$ or PARP2$^{-/-}$ target cells. (**E**) Quantification of cleaved caspase-3 in the CD45$^-$ cells determined by flow cytometry after 4 hours of coculture of EMyc control or PARP2$^{-/-}$ cells with PARP2$^{+/+}$ or PARP2$^{-/-}$ splenocytes (ratio of 1:30) ($N = 6$ mice per group). (**F**) Quantification of cleaved caspase-3 in the CD45$^-$ cells determined by flow cytometry after 4 hours of coculture of EMyc control or PARP2$^{-/-}$ cells with PARP2$^{+/+}$ or PARP2$^{-/-}$ NK cells (ratio of 1:1) ($N = 3$ mice per group). *$P < 0.05$; **$P < 0.01$; ***$P < 0.001$, unpaired Student's t test versus PARP2$^{+/+}$.

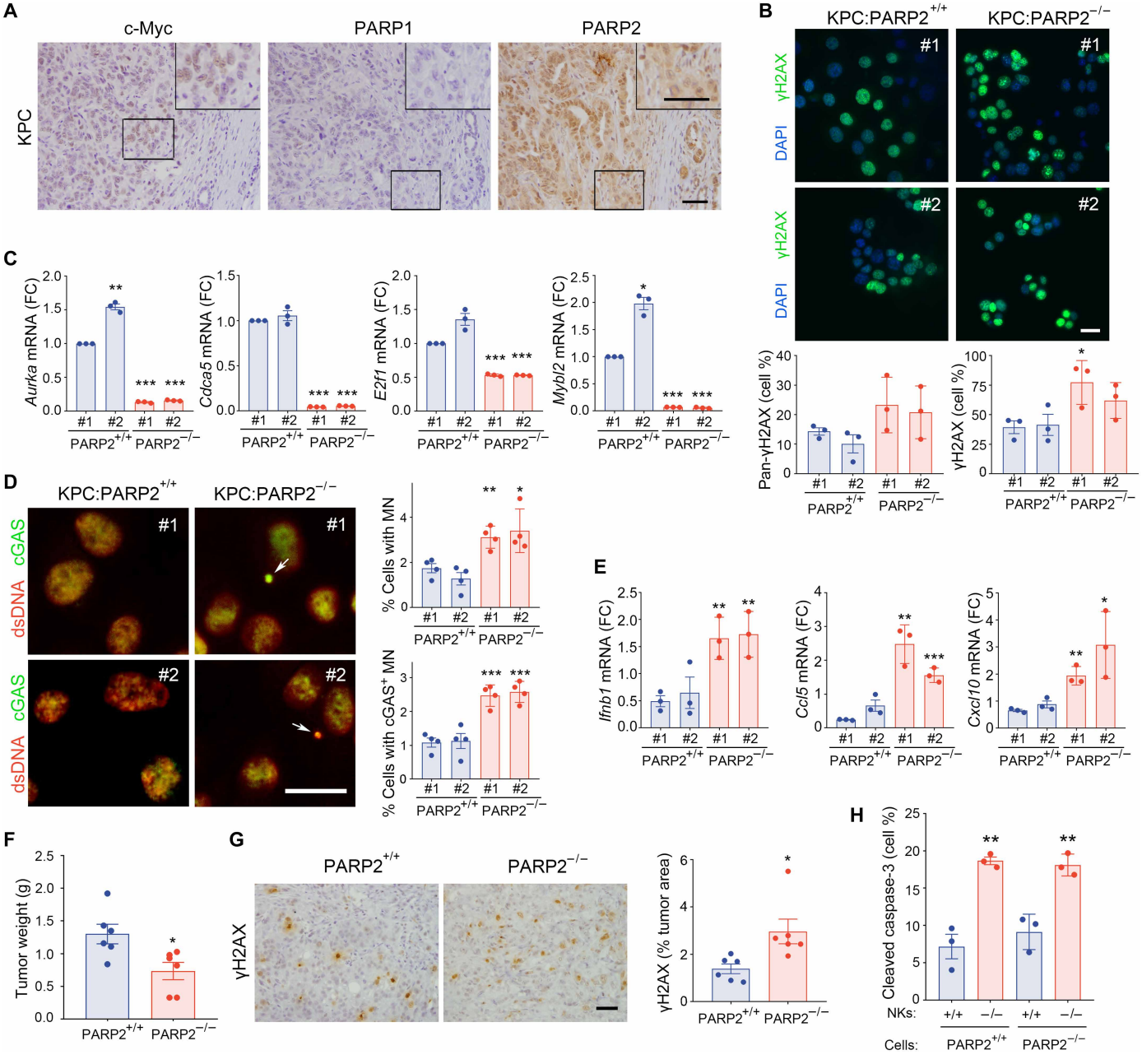

Fig. 6. PARP2 deficiency induces genomic instability and an antitumor immune response in *Kras*^{G12D}-driven pancreatic cancer. (**A**) Representative immunohistochemistry of c-Myc, PARP1, and PARP2 in serial KPC tissue sections. Scale bars, 50 μm. Insets show higher magnification views of the regions indicated by black squares. (**B**) Top: Representative immunofluorescence images of γH2AX (green) and 4′,6-diamidino-2-phenylindole (DAPI) (blue) in cisplatin-treated KPC:PARP2$^{+/+}$ and KPC:PARP2$^{-/-}$ cells. Scale bar, 25 μm. Bottom: Percentage of cells exhibiting pan-nuclear γH2AX and total γH2AX ($N = 3$). (**C**) RT-qPCR analysis of RS-related genes (*Aurka*, *Cdca5*, *E2f1*, and *Mybl2*) normalized to β-actin (*Actb*) and shown as fold change (FC) to KPC:PARP2$^{+/+}$ #1 ($N = 3$). (**D**) Left: Representative immunocytofluorescence of micronuclei, detected by cytosolic dsDNA (red), and cGAS (green) in KPC:PARP2$^{+/+}$ and KPC:PARP2$^{-/-}$ cells. Scale bar, 20 μm. Right: Percentage of cells with micronuclei (top), and percentage of cells with cGAS^{+} micronuclei (bottom). Data represent the percentage of cells from a minimum of 400 cells analyzed per group. (**E**) RT-qPCR analysis of STING-dependent genes (*Ifnb1*, *Ccl5*, and *Cxcl10*) normalized to *Actb* and shown as fold change to KPC control cells ($N = 3$). (**F**) Tumor weight after implantation of KPC:PARP2$^{+/+}$ or KPC:PARP2$^{-/-}$ cells in NSG mice ($N = 6$ per group). *$P < 0.05$, Mann-Whitney *U* test. (**G**) Representative γH2AX immunohistochemistry images (left) and quantification (right) in tumors from NSG mice injected with KPC:PARP2$^{+/+}$ and KPC:PARP2$^{-/-}$ cells ($N = 6$ per group). (**H**) Percentage of epithelial cells (CD45^{-}) positive for cleaved caspase-3 by flow cytometry after coculture with PARP2$^{+/+}$ or PARP2$^{-/-}$ NK cells (ratio of 1:1) ($N = 3$ mice per group). *$P < 0.05$; **$P < 0.01$; ***$P < 0.001$, unpaired Student's *t* test relative to PARP2$^{+/+}$ #1 [(B) to (E)] and compared with PARP2$^{+/+}$ [(G) and (H)]. Comparisons without asterisks are not significant.

γH2AX staining upon treatment with cisplatin (Fig. 6B), confirming PARP2's role in DNA damage response and RS (*20*). Furthermore, RT-qPCR analysis confirmed down-regulation of key genes from the Dreyer *et al.* RS signature (*16*) (*Aurka*, *Cdca5*, *E2f1*, and *Mybl2*) in PARP2-deficient cells (Fig. 6C), in line with impaired RS machinery activity. To further characterize the consequences of increased genomic instability upon PARP2 loss, we assessed cytosolic DNA accumulation by immunofluorescence staining of dsDNA and cGAS. KPC:PARP2$^{-/-}$ cells showed a significant increase in the number of micronuclei detected by cytosolic dsDNA compared with KPC:PARP2$^{+/+}$ (Fig. 6D and fig. S5B). Notably, a higher proportion of these micronuclei were cGAS-positive, reflecting enhanced sensing of cytosolic DNA by this innate immune sensor (Fig. 6D and fig. S5B). Consistently, phosphorylated STING (pSTING) and phosphorylated TANK-Binding Kinase 1 (pTBK1) were increased in PARP2-deficient KPC cells (fig. S5C), which also exhibited significantly elevated expression of STING-dependent genes, including *Ifnb1*, *Ccl5*, and *Cxcl10* (Fig. 6E).

Similarly to what we did in the Ela-Myc model, we also assessed the tumor-intrinsic impact of PARP2 loss in vivo in the *Kras*^{G12D}-driven model by orthotopic implantation of KPC:PARP2$^{+/+}$ or KPC:PARP2$^{-/-}$ cells into immunodeficient NSG mice. Tumors derived from PARP2$^{-/-}$ cells showed significantly reduced growth (Fig. 6F) and increased γH2AX staining by immunohistochemistry (Fig. 6G), while levels of phospho-histone H3 (Ser^{10}) and cleaved caspase-3 remained unchanged (fig. S5D), supporting a role for PARP2 in controlling RS.

Considering the key role of PARP2 in the regulation of immune response found in the Ela-Myc model and the observed up-regulation of STING-dependent genes in PARP2-deficient KPC cells, we also explored whether PARP2 depletion may affect the immune microenvironment in this *Kras*^{G12D}-driven model. To this aim, KPC:PARP2$^{+/+}$ or KPC:PARP2$^{-/-}$ cells were orthotopically implanted into PARP2$^{+/+}$ or PARP2$^{-/-}$ immunocompetent syngeneic host mice. Both KPC:PARP2$^{+/+}$ and KPC:PARP2$^{-/-}$ cells implanted in PARP2$^{-/-}$ background showed a significant increase in CD4 and CD8 T cells and B cells (fig. S6A), suggesting that systemic PARP2 loss enhances antitumor immune cell recruitment. Moreover, tumors derived from KPC:PARP2$^{-/-}$ implanted cells showed decreased immunosuppressive Arg1^{+} macrophage infiltrates (fig. S6A), independent of the host genotype.

To functionally determine the cellular cytotoxicity of immune cells against KPC tumor cells, splenocytes were isolated from the aforementioned host mice at day 21 postimplantation and cocultured with the corresponding KPC:PARP2$^{+/+}$ or KPC:PARP2$^{-/-}$ cells, following the experimental scheme depicted in Fig. 5D. Splenocytes from PARP2$^{-/-}$ mice exhibited heightened cytotoxic activity against both KPC:PARP2$^{+/+}$ and KPC:PARP2$^{-/-}$ cells (fig. S6B), suggesting that systemic PARP2 deficiency enhances the cytolytic capacity of immune effector cells. Given the short coculture duration (4 hours) and previous findings in Ela-Myc model, we next focused on NK cells. Purified NK cells from PARP2$^{-/-}$ mice also showed elevated cytotoxicity toward both KPC:PARP2$^{+/+}$ and KPC:PARP2$^{-/-}$ target cells compared with NK cells from PARP2$^{+/+}$ mice (Fig. 6H), consistent with a cell-intrinsic enhancement of NK cell function in the absence of PARP2.

Together, these results indicate that PARP2 genetic deletion promotes antitumor immunity in *Kras*^{G12D}-driven pancreatic cancer by reshaping the tumor microenvironment and enhancing NK cytotoxic responses.

DISCUSSION

Identifying new molecular targets for effective treatments is an urgent need in pancreatic cancer. Precision medicine is reshaping the landscape of cancer treatment through more effective and less toxic therapies. One of the most recent therapeutic breakthroughs in PDAC has been the approval of PARPi, although its use is restricted to patients with *BRCA1/2* mutations, and the impact is only modest (*9*). Another important revolution in cancer therapy is immunotherapy, although it shows limited effectiveness in immunologically "cold" tumors, like PDAC. Consequently, current efforts are focused on deciphering how to activate immune programs to convert these cancers into immunologically "hot" tumors. Here, we provide evidence that PARP2 is present both in tumor cells and in the PDAC microenvironment, and its selective deletion affects tumor progression in both *Myc*-driven and *Kras*^{G12D}-driven mouse models by accumulating RS and restoring antitumor immune surveillance. Therefore, selective PARP2 inhibition can be a promising strategy to combat PDAC and to enhance its responsiveness to immunotherapy.

Our data reveal that PARP2 depletion delays pancreatic tumor progression and increases survival through both tumor cell–intrinsic and –extrinsic mechanisms (Fig. 7). On the one hand, we demonstrate that PARP2 expression in tumor cells plays a key role in maintaining genomic integrity in PDAC. Using a *Myc*-driven preclinical model, we found that in the absence of PARP2, tumor cells accumulate RS and DNA damage and display aberrant chromosome segregation, likely resulting in mitotic catastrophe (*21*) and concomitant cell death. Myc is frequently activated in PDAC (*3*) and is a major driver of RS (*6*), which can explain the high genomic instability found in this tumor. We observed overlapping spatial distribution patterns of PARP2 and c-Myc in adjacent serial sections from human and mouse PDAC tissue samples, suggesting that high RS induced by Myc may trigger PARP2 overexpression in PDAC. In line with this, squamous tumors, which express the highest levels of PARP2 (Fig. 1C), are characterized by activation of the Myc pathway (*22*). Recent studies have pointed out RS inducers as cancer therapeutic agents, being already included in several preclinical studies (*16*, *23*) and clinical trials, also in PDAC (NCT06015659).

On the other hand, PARP2 deficiency also exerts tumor-extrinsic effects by reshaping the intratumoral environment toward an immune effector phenotype, which may also contribute to the delayed tumor growth. The contribution of PARP2 to modifying the tumor environment remains largely unknown. Emerging evidence suggests that PARP2 may not only affect cancer cell biology but also modulate the immune response to tumors, both by acting directly on immune cells and by altering signaling pathways in tumor cells that shape immune interactions (*24*). In particular, a link has been established between genomic instability and the accumulation of DNA in the cytoplasm, which, in turn, activates the STING signaling pathway, leading to type I interferon production among other immune-stimulatory signals (*25*). The interferon-α response hallmark and a STING-dependent gene signature were up-regulated in EMyc:PARP2$^{-/-}$ pancreatic samples and in KPC:PARP2$^{-/-}$ cells, suggesting the involvement of these pathways in the modulation of immune response mediated by PARP2 loss. Moreover, in vitro functional assays revealed that immune cells from PARP2-deficient hosts, specifically total splenocytes and purified NK cells from EMyc:PARP2$^{-/-}$ and KPC:PARP2$^{-/-}$ mice, exhibited enhanced antitumor

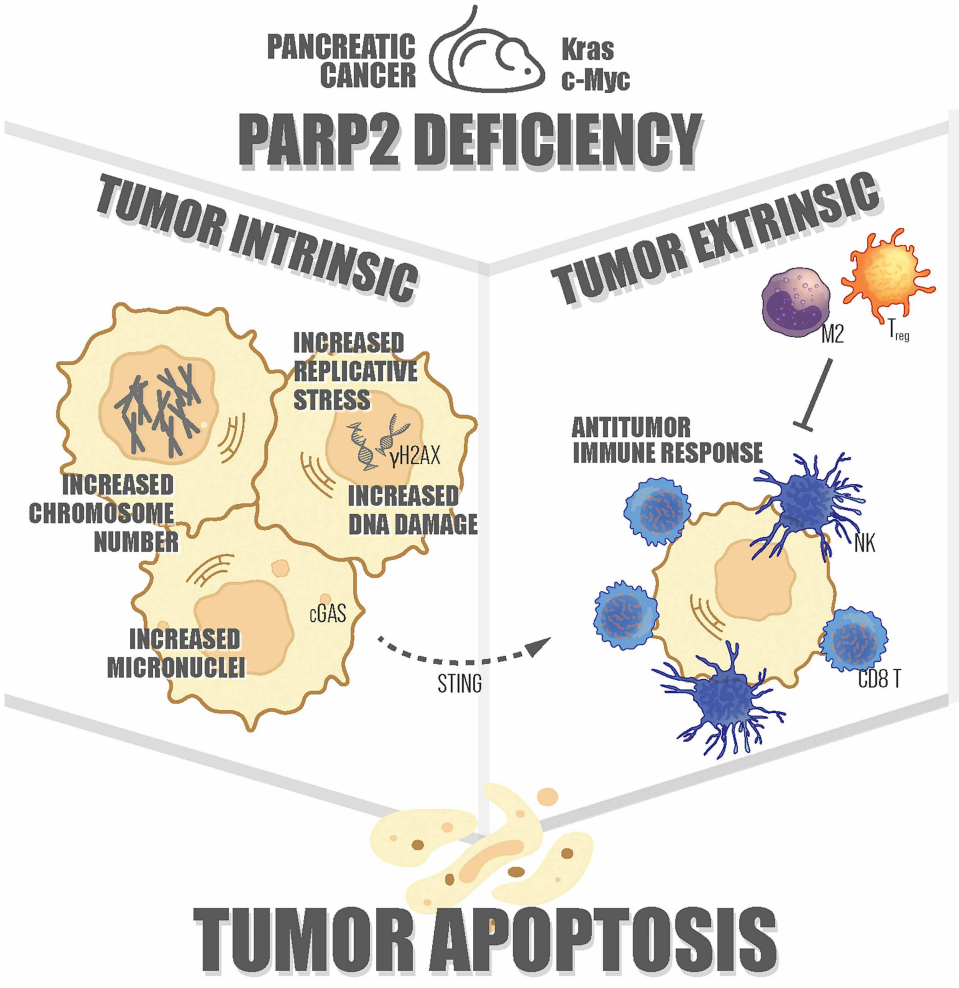

Fig. 7. Working model of PARP2 deficiency–mediated tumor suppression in pancreatic cancer through intrinsic and extrinsic mechanisms. Schematic representation of how PARP2 loss, investigated in both *Kras*^{G12D}-driven and *Myc*-driven murine pancreatic cancer tumor models, results in a combination of tumor cell–intrinsic and –extrinsic effects. Intrinsically, PARP2 deficiency leads to increased RS, accumulation of DNA damage, formation of micronuclei, and elevated chromosomal instability. These genomic perturbations contribute to heightened tumor cell vulnerability and apoptosis. Extrinsically, PARP2-deficient tumors exhibit enhanced recruitment of antitumor immune cells, coupled with exclusion of immunosuppressive T_{reg} cells and M2 macrophages, thereby fostering a proinflammatory microenvironment that facilitates immune-mediated tumor clearance. Together, these mechanisms underpin the tumor-suppressive effects observed upon PARP2 loss.

activity. These results suggest a cell-intrinsic enhancement of immune effector function upon PARP2 loss, leading to a systemic activation that likely cooperates with tumor-intrinsic STING signaling to amplify antitumor immunity (Fig. 7). In line with this, Myc and KRAS have been shown to suppress the type I interferon pathway in PDAC to evade B and NK cell–mediated immunity (*26*), supporting our model, whereby PARP2 loss reverses this immunosuppressive program and promotes antitumor immune responses. Notably, STING agonists have been shown to promote potent NK cell–mediated tumor rejection independently of $CD8^+$ T cells, highlighting the potential of targeting the STING-NK axis in tumors that resist classical T cell–based immunotherapies (*27*). Future studies will help to elucidate the relative contribution of these mechanisms (RS-induced, STING-dependent type I interferon production, and systemic immune activation) to the enhanced antitumor immune response observed upon PARP2 loss in pancreatic cancer. In addition, while our experiments with immunodeficient mice delineate a clear tumor cell–intrinsic requirement for PARP2 in maintaining genomic integrity, we acknowledge that additional mechanistic in vivo approaches would be necessary to fully quantify the relative contribution of tumor-intrinsic versus host-mediated effects. Nevertheless, our data strongly support a dual model whereby PARP2 loss compromises tumor cell fitness while simultaneously enhancing antitumor immunity, suggesting that PARP2 inhibition may hold therapeutic value independently of tumor cell PARP2 levels.

An alternative pathway potentially involved in immune regulation after PARP2 depletion is related to galectin-driven immunoregulatory circuits, particularly those mediated by galectins-1, -3, and -9, which are known to influence pancreatic cancer progression (*28*–*30*). RNA-seq analysis (GSE2777055) suggests altered expression of Gal-3 and Gal-9 in early tumor lesions, a finding consistent with the observed heightened antitumor immune responses. While these insights warrant further experimental validation, they align with the well-established role of galectins in shaping the tumor immune microenvironment.

Despite these mechanisms induced by PARP2 depletion in the *Myc*-driven model, pancreatic cells develop strategies to overcome the increased genomic instability and evade effector immune response, becoming tumorigenic. Although there is a significant delay in progression, which is associated with increased survival, all EMyc:PARP2$^{-/-}$ mice eventually develop pancreatic tumors. Notably, 80% of PARP2-deficient tumors exhibited p53 alterations, whereas less than 20% of wild-type tumors did. These results suggest that inactivation of *Trp53*, either through loss of heterozygosity or truncating mutations, or through a missense/stabilizing mutation, is a common event in tumors arising in the absence of PARP2. Thus, the loss of p53 function likely represents a compensatory mechanism that enables tumor cells to tolerate the increased RS and genomic instability caused by the absence of PARP2, thereby sustaining tumor progression. Recent data have shown that, in addition to RS, aberrant ribosome biogenesis favors the selection of p53 mutations (*31*). Our GSEA of differentially expressed pathways between EMyc:PARP2$^{-/-}$ and EMyc:PARP2$^{+/+}$ pancreatic samples revealed that ribosome biogenesis is among the most significantly altered pathways, suggesting that it can also fuel loss of p53 function when PARP2 is inhibited. These data suggest that p53 inactivation induced after PARP2 loss is primarily tumor cell intrinsic. However, since our analyses were performed on tumors arising in EMyc:PARP2$^{-/-}$ mice, we cannot formally rule out that tumor cell–extrinsic mechanisms may also contribute.

The loss of function of p53 in late-stage EMyc:PARP2$^{-/-}$ pancreatic tumors aligns with previous results of our group suggesting that activation of p53-dependent cytostatic and apoptotic signals is critical for preventing lymphoma onset in PARP2-deficient mice (*11*). Consistent with these findings, transcriptomic analysis of preneoplastic pancreatic samples from 3-month-old EMyc:PARP2$^{-/-}$ mice revealed higher p53 pathway activation compared with EMyc:PARP2$^{+/+}$ controls, suggesting that increased early p53 activation may impose selective pressure to inactivate this pathway during tumor development. Our whole genome analysis of 2565 patients from International Cancer Genome Consortium (ICGC)/TCGA using cBIOPORTAL pan cancer has shown a significant co-occurrence of *PARP2* and *TP53* mutations (*32*). These results may enhance our understanding of the molecular mechanisms responsible for PARPi resistance in patients, which is a frequent event, either innate or acquired. Furthermore, p53 alterations in EMyc:PARP2$^{-/-}$ tumors may contribute to immune evasion, as loss or mutation of this protein can lead to dysregulation of cytokine production, reduced major histocompatibility complex class I expression, and increased recruitment of T_{reg} cells, among other mechanisms (*33*). However, our data from the *Kras*^{G12D} model, a p53-deficient model, indicate that additional mechanisms beyond p53 contribute to the modulation of immune landscape by PARP2 genetic deletion, as we observed efficient KPC:PARP2$^{-/-}$ tumor cell killing despite the potential immune evasion mechanisms associated with dysfunctional p53 signaling.

Although it is undeniable that PARPi have been a milestone in the treatment of several tumors, their clinical use has not fully met initial expectations. The anticipated synergistic efficacy of combining PARPi with DNA-damaging treatments such as chemotherapy or radiotherapy has been overshadowed by the resultant severe toxicity, limiting the clinical success of these combination strategies. Consequently, PARPi are approved only as monotherapies for cancers with deficiencies in homologous recombination, such as those harboring *BRCA1/2* mutations, limiting their use to a small patient subset. Specifically, less than 5% of patients with PDAC have this mutation, and, even within this group, the reported benefits are modest (*9*). Moreover, PARPi can cause important adverse effects, particularly hematological toxicities, reducing overall effectiveness. Notably, currently approved PARPi are nonspecific, targeting both PARP1 and PARP2. However, our data, along with previous work, strengthen the notion that each PARP member displays specific, nonredundant functions, highlighting the necessity to develop next-generation PARP selective inhibitors.

There is growing interest in the development of isoform-specific PARP inhibitors. For instance, saruparib (AZD5305), a highly selective PARP1 inhibitor, has demonstrated improved tolerability and encouraging antitumor activity in preclinical and early-phase clinical trials, specifically in tumors harboring homologous recombination deficiencies (*34*–*37*). These findings support the clinical feasibility of selective PARP targeting. Our data further broaden this therapeutic perspective by highlighting the potential relevance of PARP2-specific inhibition in pancreatic cancer. In line with this concept, we previously showed that PARP1 deletion in a *Myc*-driven model, despite promoting tumor necrosis and reducing cell proliferation, angiogenesis, and ADM, did not alter overall tumor progression or survival (*12*). In contrast, we found here that specific inactivation of PARP2 has a clear protective effect in both the same model and a *Kras*^{G12D}-driven model, supporting a selective role for PARP2 in promoting pancreatic cancer progression. Consistent with this, our experiments using the clinically approved PARP1/2 inhibitor olaparib failed to replicate the protective effects of PARP2 deletion, as olaparib treatment did not alter tumor onset or burden in either EMyc:PARP2$^{+/+}$ or EMyc:PARP2$^{-/-}$ mice. These findings further highlight the potential benefit of developing PARP2-selective inhibitors. Notably, these differences between PARP1 and PARP2 in oncogenesis have also been observed in a preclinical model of B cell lymphoma, where the loss of PARP2 prevents *Myc*-driven lymphomagenesis, whereas PARP1 deficiency accelerates it (*11*). In addition, recent findings also indicate that PARP2, but not PARP1, is a promising therapeutic target in prostate cancer (*38*).

Collectively, our work identifies PARP2 as a previously unidentified vulnerability in PDAC, supporting the notion that PARP2-selective inhibitors may offer substantial advantages over currently approved nonspecific PARPi. Specifically, (i) they will exhibit less toxicity by preserving PARP1's physiological functions; (ii) they will be effective in high RS tumors regardless of *BRCA* status, thereby significantly expanding the number of eligible patients; and (iii) they could help reverse immune tolerance, complementing and potentially synergizing with immunotherapy (*39*, *40*). This last aspect is particularly crucial in immunologically "cold" tumors like pancreatic cancer, where an immunosuppressive microenvironment poses a substantial hurdle to controlling progression and hampers the efficacy of immunotherapy. Notwithstanding, developing PARP2-specific inhibitors remains at a very early stage, with no compound currently in clinical evaluation. This represents a limitation of the current study, as we relied on genetic inactivation models and on the use of the clinically approved pan-PARP inhibitor olaparib to interrogate PARP2-specific functions. Moreover, although beyond the scope of the present work, resistance mechanisms, including those linked to p53 status, may influence treatment response and warrant further investigation to better define patient subsets most likely to benefit from PARP2-targeted therapies. Therefore, future research will be needed to validate the therapeutic efficacy of pharmacological PARP2 inhibition, potentially transforming the therapeutic landscape for PDAC and other hard-to-treat cancers.

MATERIALS AND METHODS

Experimental design

The objective of this study was to investigate the role of PARP2 in PDAC by exploring its impact on tumor progression, immune response, and genomic stability using both human samples and preclinical mouse models. We first assessed PARP2 expression in human PDAC tissues, finding it significantly up-regulated in tumors compared with normal pancreatic tissue, with higher levels in the aggressive squamous subtype. To examine the functional role of PARP2 in vivo, we used two mouse models: the *Myc*-driven Ela-Myc model and the KPC model. Upon PARP2 depletion, Ela-Myc mice exhibited delayed tumor progression. PARP2 deficiency induced RS and genomic instability, with increased DNA damage, disrupted chromosomal segregation, increased formation of micronuclei with cGAS, and enhanced p53 activity. We analyzed the tumor immune microenvironment through RNA-seq and immunohistochemistry, revealing increased infiltration of antitumor immune cells (CD4 and CD8 T cells and NK cells) and reduced protumoral macrophages and T_{reg} cells in PARP2-deficient tumors. Functional experiments determined that NK cells from PARP2-deficient mice were more cytotoxic. Both tumor-intrinsic and tumor-extrinsic related functions of PARP2 were confirmed in a $Kras^{G12D}$-driven model. Collectively, these results highlight the dual role of PARP2 in both modulating the immune landscape and maintaining genomic stability, positioning it as a potential therapeutic target to enhance immune response and hinder tumor progression in pancreatic cancer.

Human pancreatic samples

Paraffin-embedded pancreatic tissue samples were obtained from Hospital del Mar Biobank (MARBiobanc), Barcelona, Spain. Clinicopathological characteristics are described in table S1 (gender, age, and tumor stage). All participants signed an informed consent following procedures approved by the Hospital del Mar Ethical Committee for Clinical Research (2020/9067/I and 2023/11070/I).

Mice and cell lines

Animal procedures were approved by the local Animal Experimentation Ethics Committee at Parc de Recerca Biomèdica de Barcelona (PRBB), Barcelona (PNM-16-0009 and PNM-24-0012) and Comunidad de Madrid (PROEX 289/14). *Ela-Myc* mice were provided by E. Sandgren (University of Wisconsin-Madison, Madison, WI), and $PARP2^{-/-}$ mice were provided by G. de Murcia (Centre National de la Recherche Scientifique, Strasbourg, France). Ela-Myc, $PARP2^{-/-}$, and KPC mice have been described previously (*41*–*43*). Animals, all in a C57BL/6J background (RRID:IMSR_JAX:000664), were housed under pathogen-free conditions, and experimental procedures were performed following institutional guidelines for the welfare of experimental animals and guidelines for Ethical Conduct in the Care and Use of Animals, as stated by the Council for International Organizations of Medical Sciences (CIOMS). Littermates were assessed for *Myc* oncogene presence and PARP2 status after mouse weaning by earsnip DNA extraction and PCR analysis (*11*, *44*). Spontaneous pancreatic tumor growth from male and female EMyc:$PARP2^{+/+}$ (control group, $N = 28$ mice) and EMyc:$PARP2^{-/-}$ mice (experimental group, $N = 32$ mice) was followed from date of birth. Mice breeding strategy followed our previously published design (*12*). To compute a priori the required sample size (experimental units) for this procedure, G*Power 3.1.9.4 was used, applying the following criteria: two-tailed *t* test for two independent means with an effect size of 0.9, α error of 0.05, and power of 0.9. Animals with malocclusion or whose euthanasia was not directly related to tumor development were excluded from the analysis. Ethical endpoints were determined following a modified version of the criteria proposed by Morton and Griffiths (*45*). Mice were monitored daily for signs of distress, and animals were euthanized when exhibiting evident signs of cachexia or critical clinical parameters such as lack of movement, abnormal posture, ruffled fur, or dehydration. We applied a scoring system that evaluated physical appearance, weight loss, body condition, involuntary behaviors, respiratory signs, tumor size, and presence of lesions. Each category was scored from 0 to 3, with a maximum cumulative score of 14. Animals reaching a score of 3 in any single parameter, or a total score of 10 or above, were euthanized immediately. For scores between 5 and 9, supportive measures were introduced (e.g., soft food, thermal support, and analgesia), and animals were reassessed after 72 hours; if no improvement was observed, euthanasia was performed. These measures ensured rigorous and humane endpoint determination throughout the study. Life-span increase was determined based on mean survival days of 137 for EMyc:$PARP2^{+/+}$ and 196 for EMyc:$PARP2^{-/-}$ mice, using the formula $(196 - 137)/137 \times 100 = 43\%$. During necropsies, pancreatic tumors and mouse liver and lungs were weighed and fixed in 4% buffered formalin, dehydrated, and embedded in paraffin. A sample for RNA preservation was also collected in RNAlater (Sigma-Aldrich). Primary tumor pancreatic cells were established from EMyc:$PARP2^{+/+}$ and EMyc:$PARP2^{-/-}$ mice treating tissue with collagenase (1 mg/ml) and a GentleMACS dissociator. For the mutant $Kras^{G12D}$-driven model, cells derived from the KPC transgenic mouse model (*pdx1-Cre;*$Kras^{G12D}p53^{lox/+}$) were transfected with CRISPR-Cas9 knockout plasmids for PARP2, containing green fluorescent protein (GFP; Santa Cruz Biotechnology), using a transfer reagent kit (Santa Cruz Biotechnology) according to the manufacturer's instructions. GFP^+ KPC:$PARP2^{-/-}$ clones were selected by single-cell sorting and expanded. PARP2 deficiency was confirmed by Western blot. The same strategy was used to generate Ela-Myc–derived PARP2 knockout cells. Two control clones (#1 and #2 $PARP2^{+/+}$) and two PARP2 knockout clones (#1 and #2 $PARP2^{-/-}$) were selected for functional analyses. Cells were cultured in Dulbecco's modified Eagle's medium supplemented with 10% fetal bovine serum, 5% CO_2 at 37°C, and checked for mycoplasm contamination every month.

Olaparib administration

Ela-Myc transgenic mice were enrolled into treatments at 10 weeks of age. Mice were randomized to receive either olaparib (Selleckchem) or vehicle, which were administered intraperitoneally at 50 mg/kg/day for 3 weeks. Mice were monitored throughout the treatment period for changes in body weight and overall health.

Orthotopic pancreatic cancer mouse model and coculture systems

For immunodeficient mice, Ela-Myc (1 million) or KPC (50,000 cells) control cells or those knocked out for PARP2 by CRISPR-Cas9 technology (two clones for each condition) were implanted orthotopically into adult male NSG mice ($N = 6$ per group) or syngeneic C57BL/6J $PARP2^{+/+}$ or $PARP2^{-/-}$ recipient mice. Animals with leakage during orthotopic implantation or excessive bleeding during surgery were excluded from the analysis. Ethical endpoints were determined following a modified version of the criteria proposed by Morton and Griffiths (*45*), as previously detailed. Tumor growth was monitored

for 21 days, and pancreatic tumors and spleen were collected. Tumors were weighed and fixed in buffered formalin for further analysis. Spleens were dissociated, and splenocytes were isolated using a 100-μm pore size cell strainer. Cocultures were established with 50,000 KPC:PARP2$^{+/+}$ or KPC:PARP2$^{-/-}$ cells and 1.5 × 10^6 PARP2$^{+/+}$ or PARP2$^{-/-}$ splenocytes (ratio of 1:30) for 4 hours. NK cells were isolated from splenocytes by negative selection using the NK Cell Isolation Kit (Miltenyi Biotec), according to the manufacturer's instructions. NK purification was determined by flow cytometry and considered appropriate if over 80%, with less than 1% of CD3 T cell contamination [phycoerythrin-conjugated NK1.1 (BD Biosciences catalog no. 553165, RRID:AB_394677) and anaphase-promoting complex Cy7-conjugated CD3 (BD Biosciences catalog no. 560590, RRID:AB_1727461)]. NK cells were cocultured with 50,000 KPC:PARP2$^{+/+}$ or KPC:PARP2$^{-/-}$ (ratio of 1:1) for 4 hours. Cells were stained with fluorescein isothiocyanate–conjugated cleaved caspase-3 (Asp^{175}) (C92-605, BD Biosciences, RRID AB_397234) and PerCP-Cy5.5–conjugated CD45 (30-F11, BD Biosciences, RRID AB_394003) antibodies and analyzed by flow cytometry. Cell acquisition was performed in a FORTESSA cytometer (BD Biosciences) and analyzed using FlowJo (TreeStar, RRID:SCR_008520) software. Data are represented as percentage of positive cells for cleaved caspase-3 within the epithelial CD45-negative population (Figs. 5, E and F, and 6H), except for fig. S6B, for which normalization relative to the group KPC:PARP2$^{+/+}$ in PARP2$^{+/+}$ hosts had to be performed. The gating strategy is presented in fig. S4.

Histopathological assessment and immunohistochemistry

Paraffin-embedded tissue was sectioned 3-μm thick and stained with hematoxylin and eosin (H&E) or with specific antibodies for immune-histopathological analysis. Immunohistochemistry was performed as described previously in a step-by-step protocol (*46*). CellSens software and Olympus BX61 microscope were used to acquire images. Primary antibodies used for specific tissue immunostaining were mouse monoclonal anti-PARP1 antibody (clone A6.4.12) (*47*), polyclonal anti-PARP2 (Active Motif, RRID:AB_2793328), polyclonal anti-c-Myc (Santa Cruz Biotechnology, RRID:AB_631276), anti-phospho-histone H2A.X (Ser^{139}) (γH2AX) (20E3, Cell Signaling Technologies, RRID:AB_2118009), anti-cleaved caspase-3 (Asp^{175}) (MAB835, R&D Systems, RRID:AB_2243951), anti-phospho-histone H3 (Ser^{10}) (MC463, Millipore, RRID:AB_1163440), anti-Foxp3 (FJK-16s, Thermo Fisher Scientific, AB_465936), anti-arginase1 (EPR22033-369, Abcam, RRID:AB_2895715), polyclonal anti-CD45 (Abcam, RRID:AB_442810), anti-CD4 (EPR19514, Abcam, RRID:AB_2686917), polyclonal anti-CD8 (Abcam, catalog no. ab203035, RRID: not applicable), and anti-CD20 (SP32, Abcam, RRID:AB_1139386). As secondary antibodies, ImmPRESS Peroxidase polymer reagents (RRID:AB_2631198 and AB_2336528) were used (Vector Labs).

For immunohistochemistry quantification in human sections, PARP2 was evaluated through H-score (*48*). In 3-month-old Ela-Myc tissue, γH2AX, cleaved caspase-3, and phospho-histone H3 (Ser^{10}) were evaluated with ImageJ analysis by relating the percentage of positively stained cells relative to the total cell number within the analyzed field of view. In NSG mouse sections, γH2AX, cleaved caspase-3, and phospho-histone H3 (Ser^{10}) were evaluated with ImageJ analysis by relating the area corresponding to positive signal to total tumor area (1 to 10 representative fields per sample at 10× magnification, depending on tissue availability). NSG mice without tumors were excluded from the immunohistochemical analysis. In end-stage tumors, phospho-histone H3 (Ser^{10}) is presented as number of positive nuclei per field (10 representative fields per sample at 10× magnification). γH2AX was evaluated with ImageJ analysis by relating the area corresponding to positive signal to total area in five representative fields per sample at 20× magnification. In 4-month-old Ela-Myc tumors, Arg1 and Foxp3 were evaluated by counting the number of positive cells per field (five representative fields per sample at 10×). For immune infiltrates in KPC:PARP2 tissue, numbers of positive cells for CD45, CD4, CD8, CD20, and Foxp3 were manually assessed in five representative fields per sample at 10× magnification. Arg1 was evaluated with ImageJ analysis by relating the area corresponding to positive signal to total area in five representative fields per sample at 10× magnification. For 3-month-old pancreatic tissue from Ela-Myc mice, automatic analysis including follicles and pseudofollicles was performed for CD4, CD8, and CD20 with QuPath software (*49*). Briefly, areas to be analyzed were manually selected (discarding background areas), and a model based on artificial intelligence was created and trained to obtain the total number of positive cells for each marker. Slide analysis was manually validated in situ. Foxp3 and Arg1 in 3-month-old pancreatic tissue were evaluated by assessing the number of cells per field. For tumor necrosis, we used H&E-stained slides to assess the extent of necrotic areas with an expert pathologist (Mar Iglesias). The percentage of necrosis was calculated as the necrotic area relative to the total tumor area for each sample. The percentages presented in the figures represent the mean values derived from all tumors evaluated. For the acinar and ductal composition, we analyzed H&E-stained sections of each tumor and determined the percentage of ductal versus acinar tissue with an expert pathologist (MI). The percentages presented in the figures represent the mean values derived from all tumors evaluated. Regarding metastasis, we performed a comprehensive analysis by microsectioning all available liver and lung tissues from each animal, followed by H&E staining. The entire tissue was then scanned for the presence of tumor cells, and the presence or absence of metastases was recorded. The data are reported as the percentage of animals per group with at least one histologically confirmed metastasis.

RNA expression and bioinformatics analysis

Human PARP2 RNA expression from healthy and tumor pancreas was downloaded from GTEx (167 normal tissue) and TCGA (150 primary tumors and 4 solid normal tissue). Pancreatic data on human PARP2 expression were retrieved from GTEx (RRID:SCR_013042) and TCGA (RRID:SCR_003193) (*50*). The table of counts was calculated from raw mapped counts with HTSEQ (RRID:SCR_005514). Genes having less than 1 count-per-million bases–normalized reads (approximately less than 60 reads) in at least 91 (half) of the samples were excluded from the analysis. Raw library size differences between samples were treated with the weighed "trimmed mean method" (TMM) (*51*) implemented in the edgeR package (RRID:SCR_012802) (*52*). Samples were classified into different groups according to PARP2 quartile expression, using quantile function from R. For the differential expression (DE) analysis, read counts were converted to log 2-counts-per-million (logCPM), and the mean-variance relationship was modeled with precision weights using the voom approach in LIMMA package. DE analysis was performed according to PARP2 level (low versus high). Preranked GSEA (*53*) implemented in clusterProfiler (RRID:SCR_016884) (*54*) package version 4.0.0 was used to retrieve enriched functional pathways. The

ranked list of genes was generated using the −log(*P* value) × signFC for each gene from the statistics obtained in the DE analysis with LIMMA (RRID:SCR_010943) (*55*). Functional annotation was obtained based on the enrichment of gene sets belonging to gene set collections in Molecular Signatures Database (MSigDB).

For RNA-seq analysis, pancreatic tissue was collected from 3-month-old mice ($N = 3$ EMyc:PARP2$^{+/+}$; $N = 3$ EMyc:PARP2$^{-/-}$ mice), immediately preserved in RNAlater (QIAGEN), and stored at −80°C until processing. Total RNA was extracted from the pancreas (excluding macroscopic tumor nodules, if present) by mechanical disaggregation and digestion in a tissue homogenizer with lysis buffer using the RNeasy Mini Kit (QIAGEN). RNA integrity was assessed using the Agilent Bioanalyzer (RNA Integrity Number > 9.5). Sequencing was performed in the CRG Genomics Unit (Barcelona). RNA-seq data have been deposited into the Gene Expression Omnibus (GEO; RRID:SCR_005012) under accession GSE277055. Libraries were prepared with 500 ng of RNA using the TruSeq stranded mRNA Library Prep Kit (Illumina) and were then quantified by qPCR using the KAPA Library Quantification Kit KK4835 (Roche) prior to the amplification with Illumina's cBot. Libraries were sequenced to an average depth of 38 million reads per sample on the Illumina HiSeq2500 (single-end, 50 + 8 base pair reads). All RNA samples were processed in a single batch to minimize technical variability. Quality of the raw data was checked using FastQC (RRID:SCR_014583) (version 0.11.5) (*56*), and the reads were trimmed for low quality and adapters using skewer (version 0.2.2) (*57*). The percentage of reads mapping to ribosomal RNA was assessed using riboPicker (RRID:SCR_000360) (version 0.4.3) (*58*). Raw reads were mapped to the *Mus musculus* reference genome Gencode M21 release corresponding to the Ensembl (RRID:SCR_002344) release 96 and counted at the gene level using STAR (version 2.5.3a) (*59*) and parameters "--outSAMunmapped None --outSAMtype BAM SortedByCoordinate --quantMode GeneCounts." Qualimap (RRID:SCR_001209) (version 2.2.1) (*60*) was used to check the quality of the aligned reads. DE analysis was performed in the R (*61*) Bioconductor (RRID:SCR_006442) (*62*) environment, using the DESeq2 (RRID:SCR_015687) package version 1.28.1 (*63*). As the library preparation protocol was reverse stranded, the fourth column of the STAR (RRID:SCR_005622) gene count output of each sample was taken as input for DESeq2. Genes that had less than two read counts across all samples in each analysis group were filtered out before processing the data. Principal components analysis was processed using the prcomp method from the stats core R package on the regularized log-transformed data and plotted using the ggplot2 (RRID:SCR_014601) (*64*) package. Genes were selected as significantly differentially expressed if the FDR-adjusted *P* value was less than 0.01 and the absolute log 2 fold change was more than 1.5. In addition, BEDtools (RRID:SCR_006646) version 2.26.0 (*65*) and SAMTOOLS (RRID_SCR:002105) 1.4.1 (*66*) were used. The gene enrichment analysis was performed using GSEA (RRID:SCR_003199) version 4.0.3 (*53*). For deconvolution analysis, RNA-seq data were filtered and processed through ImmuCellAI-mouse (*19*). Relative scores (represented in Fig. 5B) for each cell type and sample were directly obtained from ImmuCellAI-mouse. To assess RS, we interrogated gene sets curated from the previously published transcriptional signatures by Dreyer *et al.* and Takahashi *et al.* (*16*, *17*). To study p53 pathway activity, PROGENy package was used (*18*), a comprehensive resource containing a curated collection of pathways and their target genes, with weights for each interaction. As PROGENy uses human genes, mouse genes were annotated to human genes using orthogene package (*67*).

Reverse transcription quantitative polymerase chain reaction

Total RNA (4 μg) from each sample was used for first-strand cDNA synthesis using random hexamer primers and the RevertAid first-strand cDNA synthesis kit (Life Technologies). RT-qPCR primers were designed with Oligo Perfect Designer (Invitrogen). Primer sequences for the different genes are included in table S2. RT-qPCR was carried out using 25 ng of cDNA per sample using SYBR Green Master Mix (Applied Biosystems). Assays were run in triplicate on the ABI7900HT (Applied Biosystems) in Universitat Pompeu Fabra Genomics facility (RRID:SCR_000256). Expression levels of *Gapdh* or β-actin (*Actb*) were used to normalize the amount of the examined transcript. The relative expression levels were calculated using the comparative Ct (ΔΔCt) method. For each gene, Ct values were first normalized to the housekeeping gene to obtain ΔCt values. Then, ΔΔCt was calculated by comparing each sample to one control sample, which was arbitrarily assigned a value of 1. Fold changes in expression for all other samples were determined using the formula $2^{(-\Delta\Delta Ct)}$.

Western blot

Cells were lysed using radioimmunoprecipitation assay buffer (50 mM pH 7.5 tris-HCl, 150 mM NaCl, 1 mM EDTA, 0.1% Triton X-100, 0.1% SDS, and 1% sodium deoxycholate) supplemented with cOmplete EDTA-free protease inhibitor cocktail (Merck), 5 mM sodium fluoride (NaF), and sodium orthovanadate for protease and phosphatase enzymatic inhibition and diluted in Laemmli buffer (250 mM pH 6.8 tris-HCl, 10% SDS, 50% glycerol, 5% 2-β-mercaptoethanol, and 0.5% bromophenol blue). The protein sample (15 μg) was loaded to a 10% polyacrylamide gel, and electrophoresis and Western blot were performed. The following antibodies were used: anti-p53 (1C12, Cell Signaling Technology, RRID:AB_331743), anti-vinculin (7F9, Santa Cruz Biotechnology, RRID:AB_1131294), mouse monoclonal anti-PARP1 antibody (clone A6.4.12) (*47*), polyclonal anti-PARP2 (Active Motif, RRID:AB_2793328), polyclonal anti-β-actin (Abcam, RRID:AB_2305186), anti-pTBK1 (Cell Signaling Technology catalog no. 5483, RRID:AB_10693472), anti-TBK1 (Cell Signaling Technology catalog no. 3504, RRID:AB_2255663), anti-pSTING (Cell Signaling Technology catalog no. 72971, RRID:AB_2799831), and anti-STING (Cell Signaling Technology catalog no. 13647, RRID:AB_2732796). Horseradish peroxidase–conjugated secondary antibodies (Dako, RRID:AB_2617138 and AB_2636929) and Pierce ECL Western Blotting Substrate (Thermo Fisher Scientific) were used, and data were collected using Nine Alliance Q9 software in a UVITEC Cambridge system or Medical X-ray Blue Films (Agfa).

Immunofluorescence microscopy

For micronuclei and cGAS detection in primary EMyc:PARP2$^{+/+}$ and EMyc:PARP2$^{-/-}$ cell lines and KPC:PARP2$^{+/+}$ and KPC:PARP2$^{-/-}$ cells, cells were fixed, permeabilized with digitonin (30 μg/ml), and stained with 4′,6-diamidino-2-phenylindole (DAPI) (Merck), anti-dsDNA (Abcam catalog no. ab27156, RRID:AB_470907), and anti-cGAS (Cell Signaling Technology catalog no. 31659, RRID:AB_2799008) antibodies. Secondary antibodies used were anti-rabbit-488 immunoglobulin G (IgG) Alexa Fluor 488 (Molecular Probes catalog no. A-21206, RRID:AB_2535792) and anti-mouse IgG Alexa Fluor 555 (Thermo Fisher Scientific catalog no. A28180, RRID:AB_2536164). The number of micronuclei, total cells, and colocalization of micronuclei with cGAS

were quantified for at least 400 cells in each cell line. For γH2AX immunofluorescence, KPC:PARP2$^{+/+}$ and KPC:PARP2$^{-/-}$ cells were treated with 20 μM cisplatin (Merck) for 24 hours, fixed, stained with anti-phospho-histone H2AX (Ser^{139}) (γH2AX) (20E3, Cell Signaling Technologies, RRID:AB_2118009) and anti-rabbit-488 (Molecular Probes catalog no. A-21206, RRID:AB_2535792), and mounted with Fluoromont DAPI (SouthernBiotech). Images were taken using Nikon ECLIPSE Ni-E microscope and quantified by ImageJ. Both total γH2AX and pan-nuclear γH2AX staining were evaluated. Pan-nuclear staining was used as a marker of RS as previously described (*20*).

p53 status

Cells were treated with doxorubicin (Accord) at a final concentration of 0.5 μg/ml for 16 hours. Protein lysates were collected post-treatment, and p53 expression levels were analyzed by Western blot. Cells with intact p53 typically show increased p53 levels following treatment, while mutant or p53-deficient cells do not exhibit this response, allowing functional characterization of the p53 pathway.

Metaphase spreads

Cells were treated with colcemid (0.3 μg/ml) (Roche) for 3 hours, resuspended dropwise with 0.056 M KCl, and incubated for 5 min at 37°C. Cells were then fixed in cold methanol:glacial acetic acid solution (3:1). Cells were dropped on glass slides and stained with 3% Giemsa (Merck), and coverslips were mounted. Pictures were captured using CellSens software (RRID:SCR_008452) in an Olympus BX61 Upright Wide Field Microscope (RRID:SCR_020343) (100×). Chromosomes were counted manually with ImageJ software (RRID:SCR_003070). We manually selected and counted only those isolated nuclei in which chromosomes were appropriately spread following metaphase spread preparations. Two different primary cell lines derived from EMyc:PARP2$^{+/+}$ ($N = 15$ individual cells, each) and EMyc:PARP2$^{-/-}$ ($N = 15$ cells each) were evaluated.

Statistical analysis

Values are represented as the mean of three or more independent experiments and normalized relative to corresponding controls. Error bars in histograms correspond to the standard error of the mean (±SEM). Kaplan-Meier analyses were used for establishing survival curves, and comparisons between survival of EMyc:PARP2$^{+/+}$ and EMyc:PARP2$^{-/-}$ were performed using log-rank test, assuming independence of survival times of mice in each group. Two-group noncategorical comparisons were analyzed using unpaired two-group, two-sided Student's *t* test (assuming normal distribution) or Mann-Whitney *U* test (assuming non-normal distribution). The Pearson's chi-square test was used to determine the association between p53 deficiency and PARP2 genotype. Fisher's exact tests were applied to compare percentages (1-year survival in patients with high/low PARP2 levels; mice that survived more/less than 6 months; and mice with macroscopic tumors at the 3-month stage). Statistical analyses were performed with SPSS (RRID:SCR_002865) version 12.0.

Supplementary Materials

The PDF file includes:

Figs. S1 to S6
Tables S1 and S2
Legends for data S1 to S5

Other Supplementary Material for this manuscript includes the following:

Data S1 to S5

REFERENCES

1. R. L. Siegel, A. N. Giaquinto, A. Jemal, Cancer statistics, 2024. *CA Cancer J. Clin.* **74**, 12–49 (2024).
2. C. J. Halbrook, C. A. Lyssiotis, M. Pasca di Magliano, A. Maitra, Pancreatic cancer: Advances and challenges. *Cell* **186**, 1729–1754 (2023).
3. R. Maddipati, R. J. Norgard, T. Baslan, K. S. Rathi, A. Zhang, A. Saeid, T. Higashihara, F. Wu, A. Kumar, V. Annamalai, S. Bhattacharya, P. Raman, C. A. Adkisson, J. R. Pitarresi, M. D. Wengyn, T. Yamazoe, J. Li, D. Balli, M. J. Lariviere, T. V. C. Ngo, I. W. Folkert, I. D. Millstein, J. Bermeo, E. L. Carpenter, J. C. McAuliffe, M. H. Oktay, R. A. Brekken, S. W. Lowe, C. A. Iacobuzio-Donahue, F. Notta, B. Z. Stanger, MYC levels regulate metastatic heterogeneity in pancreatic adenocarcinoma. *Cancer Discov.* **12**, 542–561 (2022).
4. N. M. Sodir, R. M. Kortlever, V. J. A. Barthet, T. Campos, L. Pellegrinet, S. Kupczak, P. Anastasiou, L. B. Swigart, L. Soucek, M. J. Arends, T. D. Littlewood, G. I. Evan, MYC instructs and maintains pancreatic adenocarcinoma phenotype. *Cancer Discov.* **10**, 588–607 (2020).
5. E. Hessmann, G. Schneider, V. Ellenrieder, J. T. Siveke, MYC in pancreatic cancer: Novel mechanistic insights and their translation into therapeutic strategies. *Oncogene* **35**, 1609–1618 (2016).
6. E. Lecona, O. Fernandez-Capetillo, Targeting ATR in cancer. *Nat. Rev. Cancer* **18**, 586–595 (2018).
7. Y. Zeng, O. Arisa, C. J. Peer, A. Fojo, W. D. Figg, PARP inhibitors: A review of the pharmacology, pharmacokinetics, and pharmacogenetics. *Semin. Oncol.* **51**, 19–24 (2024).
8. B. Lüscher, I. Ahel, M. Altmeyer, A. Ashworth, P. Bai, P. Chang, M. Cohen, D. Corda, F. Dantzer, M. D. Daugherty, T. M. Dawson, V. L. Dawson, S. Deindl, A. R. Fehr, K. L. H. Feijs, D. V. Filippov, J. P. Gagné, G. Grimaldi, S. Guettler, N. C. Hoch, M. O. Hottiger, P. Korn, W. L. Kraus, A. Ladurner, L. Lehtiö, A. K. L. Leung, C. J. Lord, A. Mangerich, I. Matic, J. Matthews, G. L. Moldovan, J. Moss, G. Natoli, M. L. Nielsen, M. Niepel, F. Nolte, J. Pascal, B. M. Paschal, K. Pawłowski, G. G. Poirier, S. Smith, G. Timinszky, Z. Q. Wang, J. Yélamos, X. Yu, R. Zaja, M. Ziegler, ADP-ribosyltransferases, an update on function and nomenclature. *FEBS J.* **289**, 7399–7410 (2022).
9. H. L. Kindler, P. Hammel, M. Reni, E. Van Cutsem, T. Macarulla, M. J. Hall, J. O. Park, D. Hochhauser, D. Arnold, D.-Y. Oh, A. Reinacher-Schick, G. Tortora, H. Algül, E. M. O'Reilly, S. Bordia, D. McGuinness, K. Cui, G. Y. Locker, T. Golan, Overall survival results from the POLO trial: A phase III study of active maintenance olaparib versus placebo for germline BRCA-mutated metastatic pancreatic cancer. *J. Clin. Oncol.* **40**, 3929–3939 (2022).
10. M. Szántó, J. Yélamos, P. Bai, Specific and shared biological functions of PARP2—Is PARP2 really a lil' brother of PARP1? *Expert Rev. Mol. Med.* **26**, e13 (2024).
11. M. A. Galindo-Campos, N. Lutfi, S. Bonnin, C. Martínez, T. Velasco-Hernandez, V. García-Hernández, J. Martín-Caballero, C. Ampurdanés, R. Gimeno, L. Colomo, G. Roué, G. Guilbaud, F. Dantzer, P. Navarro, M. Murga, O. Fernández-Capetillo, A. Bigas, P. Menéndez, J. E. Sale, J. Yélamos, Distinct roles for PARP-1 and PARP-2 in c-Myc–driven B-cell lymphoma in mice. *Blood* **139**, 228–239 (2022).
12. N. Martínez-Bosch, M. Iglesias, J. Munné-Collado, C. Martínez-Cáceres, M. Moreno, C. Guerra, J. Yélamos, P. Navarro, Parp-1 genetic ablation in Ela-myc mice unveils novel roles for Parp-1 in pancreatic cancer. *J. Pathol.* **234**, 214–227 (2014).
13. P. Bailey, D. K. Chang, K. Nones, A. L. Johns, A.-M. Patch, M.-C. Gingras, D. K. Miller, A. N. Christ, T. J. C. Bruxner, M. C. Quinn, C. Nourse, L. C. Murtaugh, I. Harliwong, S. Idrisoglu, S. Manning, E. Nourbakhsh, S. Wani, L. Fink, O. Holmes, V. Chin, M. J. Anderson, S. Kazakoff, C. Leonard, F. Newell, N. Waddell, S. Wood, Q. Xu, P. J. Wilson, N. Cloonan, K. S. Kassahn, D. Taylor, K. Quek, A. Robertson, L. Pantano, L. Mincarelli, L. N. Sanchez, L. Evers, J. Wu, M. Pinese, M. J. Cowley, M. D. Jones, E. K. Colvin, A. M. Nagrial, E. S. Humphrey, L. A. Chantrill, A. Mawson, J. Humphris, A. Chou, M. Pajic, C. J. Scarlett, A. V. Pinho, M. Giry-Laterriere, I. Rooman, J. S. Samra, J. G. Kench, J. A. Lovell, N. D. Merrett, C. W. Toon, K. Epari, N. Q. Nguyen, A. Barbour, N. Zeps, K. Moran-Jones, N. B. Jamieson, J. S. Graham, F. Duthie, K. Oien, J. Hair, R. Grützmann, A. Maitra, C. A. Iacobuzio-Donahue, C. L. Wolfgang, R. A. Morgan, R. T. Lawlor, V. Corbo, C. Bassi, B. Rusev, P. Capelli, R. Salvia, G. Tortora, D. Mukhopadhyay, G. M. Petersen, D. M. Munzy, W. E. Fisher, S. A. Karim, J. R. Eshleman, R. H. Hruban, C. Pilarsky, J. P. Morton, O. J. Sansom, A. Scarpa, E. A. Musgrove, U.-M. H. Bailey, O. Hofmann, R. L. Sutherland, D. A. Wheeler, A. J. Gill, R. A. Gibbs, J. V. Pearson, N. Waddell, A. V. Biankin, S. M. Grimmond, S. M. Grimmond, Genomic analyses identify molecular subtypes of pancreatic cancer. *Nature* **531**, 47–52 (2016).
14. P. J. Grippo, E. P. Sandgren, Acinar-to-ductal metaplasia accompanies c-myc-induced exocrine pancreatic cancer progression in transgenic rodents. *Int. J. Cancer* **131**, 1243–1248 (2012).
15. J. Farrés, L. Llacuna, J. Martin-Caballero, C. Martínez, J. J. Lozano, C. Ampurdanés, A. J. López-Contreras, L. Florensa, J. Navarro, E. Ottina, F. Dantzer, V. Schreiber, A. Villunger, O. Fernández-Capetillo, J. Yélamos, PARP-2 sustains erythropoiesis in mice by limiting replicative stress in erythroid progenitors. *Cell Death Differ.* **22**, 1144–1157 (2015).
16. S. B. Dreyer, R. Upstill-Goddard, V. Paulus-Hock, C. Paris, E.-M. Lampraki, E. Dray, B. Serrels, G. Caligiuri, S. Rebus, D. Plenker, Z. Galluzzo, H. Brunton, R. Cunningham, M. Tesson, C. Nourse, U.-M. Bailey, M. Jones, K. Moran-Jones, D. W. Wright, F. Duthie, K. Oien, L. Evers, C. J. M. Kay, G. A. McGregor, A. Gulati, R. Brough, I. Bajrami, S. Pettitt, M. L. Dziubinski,

J. Candido, F. Balkwill, S. T. Barry, R. Grützmann, L. Rahib, Glasgow Precision Oncology Laboratory, Australian Pancreatic Cancer Genome Initiative, A. Johns, M. Pajic, F. E. M. Froeling, P. Beer, E. A. Musgrove, G. M. Petersen, A. Ashworth, M. C. Frame, H. C. Crawford, D. M. Simeone, C. Lord, D. Mukhopadhyay, C. Pilarsky, D. A. Tuveson, S. L. Cooke, N. B. Jamieson, J. P. Morton, O. J. Sansom, P. J. Bailey, A. V. Biankin, D. K. Chang, Targeting DNA damage response and replication stress in pancreatic cancer. *Gastroenterology* **160**, 362–377.e13 (2021).
17. N. Takahashi, S. Kim, C. W. Schultz, V. N. Rajapakse, Y. Zhang, C. E. Redon, H. Fu, L. Pongor, S. Kumar, Y. Pommier, M. I. Aladjem, A. Thomas, Replication stress defines distinct molecular subtypes across cancers. *Cancer Res. Commun.* **2**, 503–517 (2022).
18. M. Schubert, B. Klinger, M. Klünemann, A. Sieber, F. Uhlitz, S. Sauer, M. J. Garnett, N. Blüthgen, J. Saez-Rodriguez, Perturbation-response genes reveal signaling footprints in cancer gene expression. *Nat. Commun.* **9**, 20 (2018).
19. Y. R. Miao, M. Xia, M. Luo, T. Luo, M. Yang, A. Y. Guo, ImmuCellAI-mouse: A tool for comprehensive prediction of mouse immune cell abundance and immune microenvironment depiction. *Bioinformatics* **38**, 785–791 (2022).
20. M. Murga, S. Campaner, A. J. Lopez-Contreras, L. I. Toledo, R. Soria, M. F. Montaña, L. D'Artista, T. Schleker, C. Guerra, E. Garcia, M. Barbacid, M. Hidalgo, B. Amati, O. Fernandez-Capetillo, Exploiting oncogene-induced replicative stress for the selective killing of Myc-driven tumors. *Nat. Struct. Mol. Biol.* **18**, 1331–1335 (2011).
21. I. Vitale, L. Galluzzi, M. Castedo, G. Kroemer, Mitotic catastrophe: A mechanism for avoiding genomic instability. *Nat. Rev. Mol. Cell Biol.* **12**, 385–392 (2011).
22. Y. Ohara, W. Tang, H. Liu, S. Yang, T. H. Dorsey, H. Cawley, P. Moreno, R. Chari, M. R. Guest, A. Azizian, J. Gaedcke, M. Ghadimi, N. Hanna, S. Ambs, S. P. Hussain, SERPINB3-MYC axis induces the basal-like/squamous subtype and enhances disease progression in pancreatic cancer. *Cell Rep.* **42**, 113434 (2023).
23. A. Lumeau, N. Bery, A. Frances, M. Gayral, G. Labrousse, C. Ribeyre, C. Lopez, A. Nevot, A. El Kaoutari, N. Hanoun, E. Sarot, M. Perrier, F. Pont, J.-P. Cerapio, J. J. Fournie, F. Lopez, M. Madrid-Mencia, V. Pancaldi, M.-J. Pillaire, V. Bergoglio, J. Torrisani, N. Dusetti, J.-S. Hoffmann, L. Buscail, M. Lutzmann, P. Cordelier, Cytidine deaminase resolves replicative stress and protects pancreatic cancer from DNA-targeting drugs. *Cancer Res.* **84**, 1013–1028 (2024).
24. L. Moreno-Lama, M. A. Galindo-Campos, C. Martínez, L. Comerma, I. Vazquez, M. Vernet-Tomas, C. Ampurdanés, N. Lutfi, J. Martin-Caballero, F. Dantzer, M. Quintela-Fandino, S. O. Ali, J. Jimeno, J. Yélamos, Coordinated signals from PARP-1 and PARP-2 are required to establish a proper T cell immune response to breast tumors in mice. *Oncogene* **39**, 2835–2843 (2020).
25. N. Samson, A. Ablasser, The cGAS-STING pathway and cancer. *Nat. Cancer* **3**, 1452–1463 (2022).
26. N. Muthalagu, T. Monteverde, X. Raffo-Iraolagoitia, R. Wiesheu, D. Whyte, A. Hedley, S. Laing, B. Kruspig, R. Upstill-Goddard, R. Shaw, S. Neidler, C. Rink, S. A. Karim, K. Gyuraszova, C. Nixon, W. Clark, A. V. Biankin, L. M. Carlin, S. B. Coffelt, O. J. Sansom, J. P. Morton, D. J. Murphy, Repression of the type i interferon pathway underlies MYC- and KRAS-dependent evasion of NK and B cells in pancreatic ductal adenocarcinoma. *Cancer Discov.* **10**, 872–887 (2020).
27. C. J. Nicolai, N. Wolf, I.-C. Chang, G. Kirn, A. Marcus, C. O. Ndubaku, S. M. McWhirter, D. H. Raulet, NK cells mediate clearance of $CD8^+$ T cell-resistant tumors in response to STING agonists. *Sci. Immunol.* **5**, eaaz2738 (2020).
28. D. Yang, X. Sun, R. Moniruzzaman, H. Wang, C. Citu, Z. Zhao, I. I. Wistuba, H. Wang, A. Maitra, Y. Chen, Genetic deletion of galectin-3 inhibits pancreatic cancer progression and enhances the efficacy of immunotherapy. *Gastroenterology* **167**, 298–314 (2024).
29. A. Quilbe, R. Mustapha, B. Duchêne, A. Kumar, E. Werkmeister, E. Leteurtre, O. Moralès, N. Jonckheere, I. Van Seuningen, N. Delhem, A novel anti-galectin-9 immunotherapy limits the early progression of pancreatic neoplastic lesions in transgenic mice. *Front. Immunol.* **14**, 1267279 (2023).
30. C. A. Orozco, N. Martinez-Bosch, P. E. Guerrero, J. Vinaixa, T. Dalotto-Moreno, M. Iglesias, M. Moreno, M. Djurec, F. Poirier, H.-J. Gabius, M. E. Fernandez-Zapico, R. F. Hwang, C. Guerra, G. A. Rabinovich, P. Navarro, Targeting galectin-1 inhibits pancreatic cancer progression by modulating tumor–stroma crosstalk. *Proc. Natl. Acad. Sci. U.S.A.* **115**, E3769–E3778 (2018).
31. M. S. Lindström, J. Bartek, A. Maya-Mendoza, p53 at the crossroad of DNA replication and ribosome biogenesis stress pathways. *Cell Death Differ.* **29**, 972–982 (2022).
32. The ICGC/TCGA Pan-Cancer Analysis of Whole Genomes Consortium, Pan-cancer analysis of whole genomes. *Nature* **578**, 82–93 (2020).
33. S. Liu, T. Liu, J. Jiang, H. Guo, R. Yang, p53 mutation and deletion contribute to tumor immune evasion. *Front. Genet.* **14**, 1088455 (2023).
34. AZD5305 more tolerable than earlier PARP agents. *Cancer Discov.* **12**, 1602 (2022).
35. G. Illuzzi, A. D. Staniszewska, S. J. Gill, A. Pike, L. McWilliams, S. E. Critchlow, A. Cronin, S. Fawell, G. Hawthorne, K. Jamal, J. Johannes, E. Leonard, R. Macdonald, G. Maglennon, J. Nikkilä, M. J. O'Connor, A. Smith, H. Southgate, J. Wilson, J. Yates, S. Cosulich, E. Leo, Preclinical characterization of AZD5305, a next-generation, highly selective PARP1 inhibitor and trapper. *Clin. Cancer Res.* **28**, 4724–4736 (2022).
36. J. W. Johannes, A. Balazs, D. Barratt, M. Bista, M. D. Chuba, S. Cosulich, S. E. Critchlow, S. L. Degorce, P. Di Fruscia, S. D. Edmondson, K. Embrey, S. Fawell, A. Ghosh, S. J. Gill, A. Gunnarsson, S. M. Hande, T. D. Heightman, P. Hemsley, G. Illuzzi, J. Lane, C. Larner, E. Leo, L. Liu, A. Madin, S. Martin, L. McWilliams, M. J. O'Connor, J. P. Orme, F. Pachl, M. J. Packer, X. Pei, A. Pike, M. Schimpl, H. She, A. D. Staniszewska, V. Talbot, E. Underwood, J. G. Varnes, L. Xue, T. Yao, K. Zhang, A. X. Zhang, X. Zheng, Discovery of 5-{4-[(7-ethyl-6-oxo-5,6-dihydro-1,5-naphthyridin-3-yl)methyl]piperazin-1-yl}-*N*-methylpyridine-2-carboxamide (AZD5305): A PARP1-DNA trapper with high selectivity for PARP1 over PARP2 and other PARPs. *J. Med. Chem.* **64**, 14498–14512 (2021).
37. A. Herencia-Ropero, A. Llop-Guevara, A. D. Staniszewska, J. Domènech-Vivó, E. García-Galea, A. Moles-Fernández, F. Pedretti, H. Domènech, O. Rodríguez, M. Guzmán, E. J. Arenas, H. Verdaguer, F. J. Calero-Nieto, S. Talbot, L. Tobalina, E. Leo, A. Lau, P. Nuciforo, R. Dienstmann, T. Macarulla, J. Arribas, O. Díez, S. Gutiérrez-Enríquez, J. V. Forment, M. J. O'Connor, M. Albertella, J. Balmaña, V. Serra, The PARP1 selective inhibitor saruparib (AZD5305) elicits potent and durable antitumor activity in patient-derived BRCA1/2-associated cancer models. *Genome Med.* **16**, 107 (2024).
38. B. Gui, F. Gui, T. Takai, C. Feng, X. Bai, L. Fazli, X. Dong, S. Liu, X. Zhang, W. Zhang, A. S. Kibel, L. Jia, Selective targeting of PARP-2 inhibits androgen receptor signaling and prostate cancer growth through disruption of FOXA1 function. *Proc. Natl. Acad. Sci. U.S.A.* **116**, 14573–14582 (2019).
39. K. Concannon, B. B. Morris, C. M. Gay, L. A. Byers, Combining targeted DNA repair inhibition and immune-oncology approaches for enhanced tumor control. *Mol. Cell* **83**, 660–680 (2023).
40. R. S. Laureano, I. Vanmeerbeek, J. Sprooten, J. Govaerts, S. Naulaerts, A. D. Garg, The cell stress and immunity cycle in cancer: Toward next generation of cancer immunotherapy. *Immunol. Rev.* **321**, 71–93 (2024).
41. E. P. Sandgren, C. J. Quaife, A. G. Paulovich, R. D. Palmiter, R. L. Brinster, Pancreatic tumor pathogenesis reflects the causative genetic lesion. *Proc. Natl. Acad. Sci.U.S.A.* **88**, 93–97 (1991).
42. J. M. de Murcia, M. Ricoul, L. Tartier, C. Niedergang, A. Huber, F. Dantzer, V. Schreiber, J.-C. Amé, A. Dierich, M. L. Meur, L. Sabatier, P. Chambon, G. de Murcia, Functional interaction between PARP-1 and PARP-2 in chromosome stability and embryonic development in mouse. *EMBO J.* **22**, 2255–2263 (2003).
43. S. R. Hingorani, E. F. Petricoin, A. Maitra, V. Rajapakse, C. King, M. A. Jacobetz, S. Ross, T. P. Conrads, T. D. Veenstra, B. A. Hitt, Y. Kawaguchi, D. Johann, L. A. Liotta, H. C. Crawford, M. E. Putt, T. Jacks, C. V. E. Wright, R. H. Hruban, A. M. Lowy, D. A. Tuveson, Preinvasive and invasive ductal pancreatic cancer and its early detection in the mouse. *Cancer Cell* **4**, 437–450 (2003).
44. N. Martínez-Bosch, M. G. Fernández-Barrena, M. Moreno, E. Ortiz-Zapater, J. Munné-Collado, M. Iglesias, S. André, H.-J. Gabius, R. F. Hwang, F. Poirier, C. Navas, C. Guerra, M. E. Fernández-Zapico, P. Navarro, Galectin-1 drives pancreatic carcinogenesis through stroma remodeling and hedgehog signaling activation. *Cancer Res.* **74**, 3512–3524 (2014).
45. D. B. Morton, P. H. Griffiths, Guidelines on the recognition of pain, distress and discomfort in experimental animals and an hypothesis for assessment. *Vet. Rec.* **116**, 431–436 (1985).
46. N. Martínez-Bosch, N. Manero-Rupérez, M. Moreno, P. Navarro, Exploring the role of galectins in cancer: In vitro and in vivo approaches. *Methods Mol. Biol.* **2442**, 685–711 (2022).
47. S. Aoufouchi, A4.3.4, A6.4.12, B5.3.9, B15.4.13 anti-poly(ADP-ribose) polymerase. *Hybridoma* **16**, 583 (1997).
48. S. Detre, G. Saclani Jotti, M. Dowsett, A "quickscore" method for immunohistochemical semiquantitation: Validation for oestrogen receptor in breast carcinomas. *J. Clin. Pathol.* **48**, 876–878 (1995).
49. P. Bankhead, M. B. Loughrey, J. A. Fernández, Y. Dombrowski, D. G. McArt, P. D. Dunne, S. McQuaid, R. T. Gray, L. J. Murray, H. G. Coleman, J. A. James, M. Salto-Tellez, P. W. Hamilton, QuPath: Open source software for digital pathology image analysis. *Sci. Rep.* **7**, 16878 (2017).
50. Cancer Genome Atlas Research Network, Integrated genomic characterization of pancreatic ductal adenocarcinoma. *Cancer Cell* **32**, 185–203.e13 (2017).
51. M. D. Robinson, A. Oshlack, A scaling normalization method for differential expression analysis of RNA-seq data. *Genome Biol.* **11**, R25 (2010).
52. Y. Chen, A. T. L. Lun, G. K. Smyth, From reads to genes to pathways: Differential expression analysis of RNA-Seq experiments using Rsubread and the edgeR quasi-likelihood pipeline. *F1000Res.* **5**, 1438 (2016).
53. A. Subramanian, P. Tamayo, V. K. Mootha, S. Mukherjee, B. L. Ebert, M. A. Gillette, A. Paulovich, S. L. Pomeroy, T. R. Golub, E. S. Lander, J. P. Mesirov, Gene set enrichment analysis: A knowledge-based approach for interpreting genome-wide expression profiles. *Proc. Natl. Acad. Sci. U.S.A.* **102**, 15545–15550 (2005).
54. G. Yu, L. G. Wang, Y. Han, Q. Y. He, ClusterProfiler: An R package for comparing biological themes among gene clusters. *OMICS* **16**, 284–287 (2012).
55. M. E. Ritchie, B. Phipson, D. Wu, Y. Hu, C. W. Law, W. Shi, G. K. Smyth, LIMMA powers differential expression analyses for RNA-sequencing and microarray studies. *Nucleic Acids Res.* **43**, e47 (2015).

56. S. Andrews, FastQC: A Quality Control tool for High Throughput Sequence Data (2010); www.bioinformatics.babraham.ac.uk/projects/fastqc/.
57. H. Jiang, R. Lei, S.-W. Ding, S. Zhu, Skewer: A fast and accurate adapter trimmer for next-generation sequencing paired-end reads. *BMC Bioinformatics* **15**, 182 (2014).
58. R. Schmieder, Y. W. Lim, R. Edwards, Identification and removal of ribosomal RNA sequences from metatranscriptomes. *Bioinformatics* **28**, 433–435 (2012).
59. A. Dobin, C. A. Davis, F. Schlesinger, J. Drenkow, C. Zaleski, S. Jha, P. Batut, M. Chaisson, T. R. Gingeras, STAR: Ultrafast universal RNA-seq aligner. *Bioinformatics* **29**, 15–21 (2013).
60. K. Okonechnikov, A. Conesa, F. García-Alcalde, Qualimap 2: Advanced multi-sample quality control for high-throughput sequencing data. *Bioinformatics* **32**, 292–294 (2016).
61. R Core Team, R, A Language and Environment for Statistical Computing, R Foundation for Statistical Computing (2020); www.r-project.org/.
62. W. Huber, V. J. Carey, R. Gentleman, S. Anders, M. Carlson, B. S. Carvalho, H. C. Bravo, S. Davis, L. Gatto, T. Girke, R. Gottardo, F. Hahne, K. D. Hansen, R. A. Irizarry, M. Lawrence, M. I. Love, J. MaCdonald, V. Obenchain, A. K. Oleś, H. Pagès, A. Reyes, P. Shannon, G. K. Smyth, D. Tenenbaum, L. Waldron, M. Morgan, Orchestrating high-throughput genomic analysis with Bioconductor. *Nat. Methods* **12**, 115–121 (2015).
63. M. I. Love, W. Huber, S. Anders, Moderated estimation of fold change and dispersion for RNA-seq data with DESeq2. *Genome Biol.* **15**, 550 (2014).
64. H. Wickham, *ggplot2: Elegant graphics for data analysis* (Springer-Verlag, 2016); 10.1007/978-3-319-24277-4.
65. A. R. Quinlan, BEDTools: The Swiss-Army tool for genome feature analysis. *Curr. Protoc. Bioinformatics* **47**, 11.12.1–11.12.34 (2014).
66. H. Li, B. Handsaker, A. Wysoker, T. Fennell, J. Ruan, N. Homer, G. Marth, G. Abecasis, R. Durbin, 1000 Genome Project Data Processing Subgroup, The sequence alignment/map format and SAMtools. *Bioinformatics* **25**, 2078–2079 (2009).
67. B.M. Schilder, N. G. Skene, orthogene: Interspecies gene mapping (R package vesion 1.4.0), Bioconductor (2022); https://doi.org/10.18129/B9.bioc.orthogene.

Acknowledgments: We thank J. Perera (Hospital del Mar Research Institute), L. Mularoni (Bellvitge Biomedical Research Institute), and J. Ponomarenko (Centre for Genomic Regulation) for bioinformatics analyses. N.V.-B. is supported by an FPU (Formación de Profesorado Universitario) predoctoral contract from the MICIU (FPU21/0928). N.M.-B., N.V.-B., and P.N. belong to the Spanish National Research Council's Cancer Hub (Conexión Cáncer-CSIC). N.M.-B., N.V.-B., B.N.-H., C.G.L., M.R., C.G., J.Y., and P.N. belong to the Spanish Pancreatic Cancer Research Alliance (ALIPANC). **Funding:** This work was supported by the following grants: Spanish Ministry of Science, Innovation and Universities (MICIU)/Instituto de Salud Carlos III (ISCIII)-European Regional Development Fund (ERDF "A way of making Europe") grants PI20/00625 and PI23/00591 (P.N.); Spanish Ministry of Science, Innovation and Universities (MICIU)/Instituto de Salud Carlos III (ISCIII)-European Regional Development Fund (ERDF "A way of making Europe") grant PI19/00514 (C.G.); Carmen Delgado/Miguel Pérez Mateo Grants-Asociación Cancer de Páncreas and Asociación Española de Pancreatología (P.N., C.G., and J.Y.); Spanish Ministry of Science, Innovation, and Universities (MICIU/AEI /10.13039/501100011033, co-funded by the European Union) grant PID2023-146049OB-I00 (J.Y.); Spanish Ministry of Science, Innovation, and Universities (MICIU) grant PID2021-127710OB-I00 (A.J.); Spanish Ministry of Science, Innovation, and Universities (MICIU) grant PID2022-136973OB-I00 (M.R.); Cancer Research Innovation in Science (CRIS) Cancer Foundation (Excellence Grant) (M.R.); Ramón y Cajal Research Fellowship grant RYC2018-025244-I (A.J.); Ministerio de Ciencia, Tecnología e Innovación (Redes Federales de Alto Impacto) (G.A.R.); and Sales and Baron Foundations (G.A.R.).

Author contributions: Conceptualization: N.M.-B., N.M.-R., C.G., G.A.R., J.Y., and P.N. Data curation: N.M.-B., N.M.-R., J.Y., and P.N. Formal analysis: N.M.-B., N.M.-R., B.N.-H., N.L., E.A., M.I., M.M.-E., A.J., G.A.R., J.Y., and P.N. Funding acquisition: G.A.R., J.Y., and P.N. Investigation: N.M.-B., N.M.-R., C.G.L., C.M., M.M., C.A., M.M.-E., J.Y., and P.N. Methodology: N.M.-B., N.M.-R., N.V.-B., B.N.-H., C.V.-B., N.L., C.M., M.M., E.A., M.I., M.M.-E., A.J., and J.Y. Project administration: J.Y. and P.N. Resources: N.M.-B., C.A., M.I., A.J., M.R., C.G., J.Y., and P.N. Supervision: A.J., J.Y., and P.N. Validation: N.M.-B., N.M.-R., M.M., C.A., M.I., M.M.-E., A.J., J.Y., and P.N. Visualization: N.M.-B., N.M.-R., C.M., A.J., G.A.R., J.Y., and P.N. Writing—original draft: N.M.-B., N.M.-R., J.Y., and P.N. Writing—review and editing: N.M.-B., N.M.-R., A.J., M.R., G.A.R., J.Y., and P.N. **Competing interests:** G.A.R. is co-founder of Galtec. The other authors declare that they have no competing interests. **Data, code, and materials availability:** All data and code needed to evaluate and reproduce the results in the paper are present in the paper and/or the Supplementary Materials. RNA-seq data have been deposited into GEO (RRID:SCR_005012) under accession GSE277055. Raw data underlying graphs from main and supplementary figures have been deposited in Zenodo (https://doi.org/10.5281/zenodo.19236810). New materials generated in this study, including biological samples and experimental resources described in Materials and Methods, are available from the corresponding authors P.N. and J.Y. (pilar.navarro@iibb.csic.es; jyelamos@researchmar.net) upon reasonable request.

Submitted 26 November 2024
Accepted 2 April 2026
Published 8 May 2026
10.1126/sciadv.adu8849

ScienceAdvances

PARP2 deficiency impairs pancreatic cancer progression by promoting genomic instability and antitumor immunity

Neus Martínez-Bosch, Noemí Manero-Rupérez, Núria Vázquez-Bellón, Bennett Nickell-Hernández, Cristina Ventura-Blanch, Nura Lutfi, Carmen G. Lechuga, Carlos Martínez, Mireia Moreno, Coral Ampurdanés, Etna Abad, Mar Iglesias, María Muñoz-Escribano, Ana Janic, Meritxell Rovira, Carmen Guerra, Gabriel A. Rabinovich, José Yélamos, and Pilar Navarro

Sci. Adv. **12** (19), eadu8849. DOI: 10.1126/sciadv.adu8849